Formation and preservation of pedogenic carbonates in South India, links with paleo-monsoon and pedological conditions: Clues from Sr isotopes, U-Th series and REEs

A. Violette, J. Riotte, J. J. Braun, P. Oliva, J. C. Marechal, M. Sekhar, C. Jeandel, S. Subramanian, Jérôme Prunier, L. Barbiero, et al.

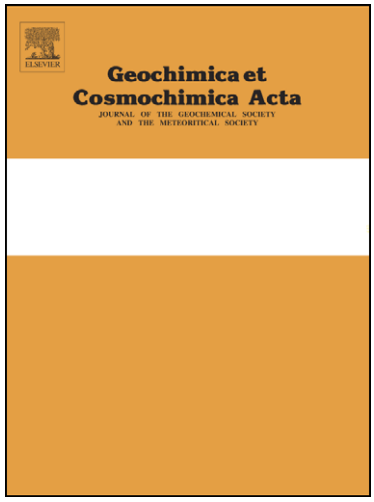

Formation and preservation of pedogenic carbonates in South India, links with paleo-monsoon and pedological conditions: Clues from Sr isotopes, U-Th series and REEs

Aurélie Violette, Jean Riotte, Jean-Jacques Braun, Priscia Oliva, Jean-Christophe Marechal, M. Sekhar, Catherine Jeandel, S. Subramanian, Jonathan Prunier, Laurent Barbiero, Bernard Dupre

PII: S0016-7037(10)00510-7
DOI: 10.1016/j.gca.2010.09.006
Reference: GCA 6917

To appear in: *Geochimica et Cosmochimica Acta*

Received Date: 27 July 2010
Accepted Date: 8 September 2010

Please cite this article as: Violette, A., Riotte, J., Braun, J-J., Oliva, P., Marechal, J-C., Sekhar, M., Jeandel, C., Subramanian, S., Prunier, J., Barbiero, L., Dupre, B., Formation and preservation of pedogenic carbonates in South India, links with paleo-monsoon and pedological conditions: Clues from Sr isotopes, U-Th series and REEs, *Geochimica et Cosmochimica Acta* (2010), doi: 10.1016/j.gca.2010.09.006

Formation and preservation of pedogenic carbonates in South India, links with paleo-monsoon and pedological conditions: Clues from Sr isotopes, U-Th series and REEs

Aurélie VIOLETTE[1, 2, 3], Jean RIOTTE[1,2,3,4] *, Jean-Jacques BRAUN[1,2,3,4], Priscia OLIVA[1,2,3], Jean-Christophe MARECHAL[1, 2, 3, 4], SEKHAR M.[4,5], Catherine JEANDEL[6], S. SUBRAMANIAN[4,7], Jonathan PRUNIER[1, 2, 3], Laurent BARBIERO[1, 2, 3], Bernard DUPRE[1,2,3]

1. Université de Toulouse ; UPS (OMP) ; LMTG ; 14, avenue Edouard Belin, F-31400 Toulouse, France
2. CNRS ; LMTG ; F-31400 Toulouse, France
3. IRD ; LMTG ; F-31400 Toulouse, France
4. Indo-French Cell for Water Sciences (IRD/IISc Joint Laboratory), Indian Institute of Science, 560012 Bangalore, India
5. Department of Civil Engineering, Indian Institute of Science, 560012 Bangalore, India
6. LEGOS, Université de Toulouse, CNRS, IRD, CNES; 14, avenue Edouard Belin, F-31400 Toulouse, France
7. Department of Materials Engineering, Indian Institute of Science, 560012 Bangalore, India

***Corresponding author: E-mail riotte@lmtg.obs-mip.fr**

1 Abstract

The influence of the pedogenic and climatic contexts on the formation and preservation of pedogenic carbonates in a climosequence in the Western Ghats (Karnataka Plateau, South West India) has been studied. Along the climosequence, the current Mean Annual Rainfall (MAR) varies within a 80 km transect from 6000 mm at the edge of the Plateau to 500 mm inland. Pedogenic carbonates occur in the MAR range of 500-1200 mm. In the semi-arid zone (MAR: 500-900 mm), carbonates occur (i) as thick hardpan calcretes on pediment slopes and (ii) as nodular horizons in polygenic black soils (i. e. vertisols). In the sub-humid zone (MAR: 900-1500 mm), pedogenic carbonates are disseminated in the black soil matrices either as loose, irregular and friable nodules of millimetric size or as indurated botryoidal nodules of centimetric to pluricentimetric size. They also occur at the top layers of the saprolite either as disseminated pluricentimetric indurated nodules or carbonate-cemented lumps of centimetric to decimetric size.

Chemical and isotopic ($^{87}Sr/^{86}Sr$) compositions of the carbonate fraction were determined after leaching with 0.25N HCl. The corresponding residual fractions containing both primary minerals and authigenic clays were digested separately and analysed. The trend defined by the $^{87}Sr/^{86}Sr$ signatures of both labile carbonate fractions and corresponding residual fractions indicates that a part of the labile carbonate fraction is genetically linked to the local soil composition. Considering the residual fraction of each sample as the most likely lithogenic source of Ca in carbonates, it is estimated that from 24 to 82% (55% on average) of Ca is derived from local bedrock weathering, leading to a consumption of an equivalent proportion of atmospheric CO_2. These values indicate that climatic conditions were humid

enough to allow silicate weathering: MAR at the time of carbonate formation likely ranged from 400 to 700 mm, which is 2- to 3-fold less than the current MAR at these locations.

The Sr, U and Mg contents and the ($^{234}U/^{238}U$) activity ratio in the labile carbonate fraction help to understand the conditions of carbonate formation. The relatively high concentrations of Sr, U and Mg in black soil carbonates may indicate fast growth and accumulation compared to carbonates in saprolite, possibly due to a better confinement of the pore waters which is supported by their high ($^{234}U/^{238}U$) signatures, and/or to higher content of dissolved carbonates in the pore waters. The occurrence of Ce, Mn and Fe oxides in the cracks of carbonate reflects the existence of relatively humid periods after carbonate formation. The carbonate ages determined by the U-Th method range from 1.33 ± 0.84 kyr to 7.5 ± 2.7 kyr and to a cluster of five ages around 20 kyr, i.e. the Last Glacial Maximum period. The young occurrences are only located in the black soils, which therefore constitute sensitive environments for trapping and retaining atmospheric CO_2 even on short time scales. The maximum age of carbonates depends on their location in the climatic gradient: from about 20 kyr for centrimetric nodules at Mule Hole (MAR = 1100 mm/yr) to 200 kyr for the calcrete at Gundlupet (MAR = 700 mm/yr, (DURAND et al., 2007)). The intensity of rainfall during wet periods would indeed control the lifetime of pedogenic carbonates and thus the duration of inorganic carbon storage in soils.

2 Introduction

The transfer of calcium and alkalinity from continents to oceans by rivers, supplied by chemical weathering of Ca-silicate minerals, and the subsequent precipitation of calcium carbonate in the oceans are known to be the major drawdown of atmospheric CO_2 on geological time scales, i. e. $\geq 10^6$ yr (BERNER and BERNER, 1987; BERNER, 1993; DUPRE et al., 2003). However, this transfer can be delayed for periods from 10^3 to 10^6 yr by the precipitation of pedogenic carbonates within semi-arid and arid landscapes (RETALLACK, 1994), which acts like a buffer reservoir for atmospheric CO_2. The inorganic carbon storage in soils is assumed to be in the range of 780 and 940 Gt (DART et al., 2007) and references therein), and thus represents about a third of the terrestrial C pool. The precipitation of carbonate within regolith is either direct from pore waters or induced by biological processes (GOUDIE, 1996) and may occur in various forms, namely powdery, nodule, rhizolith, fracture-infill, hard laminated crust (hardpan) and pisolitic crust (MACHETTE, 1985; NETTERBERG, 1980). These accumulations develop at the expense of various types of parent rocks under contrasted climates (WANG et al., 1994), though mean annual rainfall (MAR) of less than 600 mm favour these accumulations (LINTERN et al., 2006). Their occurrence is therefore closely linked to climate and has potential to serve as sensitive paleo-climatic indicators.

Understanding the dynamics of pedogenic carbonate formation, accumulation and storage should provide clues to determine the role of this component in the global C cycle and for its accurate modelling. Pedogenic carbonates have been consequently widely studied through various approaches. Quantifying the *in situ* weathering of Ca versus atmospheric inputs of Ca to the soil using Sr isotopes is a classical procedure, which permits estimates of atmospheric CO_2 consumption via pedogenesis (CAPO and CHADWICK, 1999; CHIQUET et al., 2000; CHIQUET et al., 1999; DURAND et al., 2006a; DURAND et al., 2007; HAMIDI et al., 2001; LINTERN et al., 2006; NAIMAN et al., 2000; NEYMARK et al., 2005; QUADE et al., 1995; VAN

86 DER HOVEN and QUADE, 2002). $\delta^{18}O$ and $\delta^{13}C$ have been used to determine paleo-
87 environmental conditions (PUSTOVOYTOV et al., 2007; QUAST et al., 2006). Dating attempts
88 with the U-Th series were successfully or unsuccessfully performed on pedogenic carbonates
89 (BRANCA et al., 2005; CANDY et al., 2004; CANDY et al., 2005; KELLY et al., 2000). U-Th
90 series disequilibria were also used to constrain the paleoweathering processes (NEYMARK and
91 AMELIN, 2008; NEYMARK et al., 2005). Finally, the study of major and trace elements within
92 the soil matrices and the contents of co-accumulated trace elements within pedogenic
93 carbonates, i.e. REEs, Sr and redox sensitive elements (DENNISTON et al., 1997; VANIMAN
94 and CHIPERA, 1996) have been reported to provide indications for the weathering conditions
95 prevailing during and after their formation.

96 In the Indian subcontinent, where current arid to semi arid landscapes are widespread,
97 various pedogenic carbonates have been studied, as nodules from vertisols (PAL et al., 2001;
98 SRIVASTAVA et al., 2002) or as calcrete hardpan (DURAND et al. 2006a; DURAND et al., 2007).
99 The soil climosequence of the Western Ghâts rainshadow on the Karnataka Plateau, South
100 West India was studied by (GUNNELL and BOURGEON, 1997). Along this 80 km
101 climosequence transect, the current MAR varies from 6000 mm at the edge of the Plateau to
102 500 mm inland. Pedogenic carbonates are present in the MAR range of 500-1200 mm. In the
103 semi-arid zone (MAR: 500-900 mm), pedogenic carbonates occur (i) as thick hardpan
104 calcretes on the pediment slopes and (ii) as nodular horizons in polygenic black soils of the
105 valley floors, soils with low hydraulic conductivity and high base status (DURAND et al., 2007;
106 GUNNELL and BOURGEON, 1997). In the sub-humid zone (MAR: 900-1500 mm), pedogenic
107 carbonates are present as nodules in both black soils and saprolite and also as cemented-
108 carbonate lumps in saprolite. With respect to calcite crystallization, soils of the sub-humid
109 zone are sensitive to temporal variations in precipitation and have undergone, in the past,
110 cyclic fluctuation of the MAR in response to decreases or increases of monsoon fluxes

(CANER and BOURGEON, 2001; RAJAGOPALAN et al., 1997; SUKUMAR et al., 1993).

The origin and paleoclimatic significance of the hardpan and overlying nodular horizon of the semi-arid zone has been investigated in the regions of Gundlupet and Coimbatore (DURAND et al., 2006a; DURAND et al., 2007). (DURAND et al., 2007) related the presence of calcrete to the *in situ* weathering of the Precambrian silicate basement and they proposed that the semi-arid conditions have remained fairly stable at these locations over a period longer than 200 kyr. Due to the stability of the Western Ghâts, (DURAND et al., 2007) proposed that the rain shadow in this region, and climate transect, have been present throughout the Quaternary with, however, possible lateral shifts of the sub-humid zone depending on the main rainfall fluctuations.

The present paper proposes a multi-approach study integrating petrographical, geochemical and isotopic tools to better understand the genesis and evolution of pedogenic carbonates occurring in soils of the sub-humid zone of the rain shadow of the Western Ghâts, where the current MAR is no longer favourable to pedogenic carbonate precipitation and accumulation but where nodules are still present in the regolith. The various pedogenic carbonates occurring at that place provide a unique opportunity for studying the dynamics of this carbon reservoir. We will first determine whether the Ca of soil carbonates is significantly derived from the local bedrock weathering, and subsequently whether these pedogenic carbonates constitute a sink for atmospheric CO_2. Based on their trace element content, $^{87}Sr/^{86}Sr$ isotopic ratios, ($^{234}U/^{238}U$) activity ratios and U-Th dating, the conditions of formation and preservation of pedogenic carbonates will be discussed in terms of pedogenic and climatic contexts.

3 Environmental settings

The study area is located in the Bandipur National Park, South of the Mysore Plateau, in the Gundlupet district. It corresponds to the sub-humid fringe of the climatic gradient of the

rain shadow of the Western Ghâts (Figure 1)**.** Ninety percent of the MAR is evenly distributed by the South West monsoon from June to October. Two small neighbouring and paired watersheds located in the sub-humid zone were selected as part of an integrated study of the impact of climate and human activities on the biogeochemical and hydrological cycles as detailed below:

- The pristine watershed of Mule Hole (11°72'N – 76°42'E, 4.1 km²) with a MAR of 1280 mm and an estimated potential evapotranspiration (PET) of 1030 mm (water years from 2004 to 2006, MARÉCHAL et al., 2009; RUIZ et al., 2010) is covered by a dry deciduous forest,
- The partially cultivated watershed of Maddur (11°78' N – 77°56' E, 7.2 km²) with a MAR of 830 mm and an estimated PET of 1250 mm (water years from 2005 to 2007) is covered by rainfed crops and coconut groves in the valley and scrubs and patches of deciduous forest on hilltops.

Both watersheds have similar substratum, saprolite and soil cover which have been studied in detail for the Mule Hole watershed (BARBIÉRO et al., 2010; BARBIERO et al., 2007; BRAUN et al., 2009; VIOLETTE et al., 2010). The parent material is composed of the Peninsular gneiss of the > 2.8 Ga West Dharwar craton (NAQVI and ROGERS, 1987) intermingled with much less abundant mafic to ultramafic rocks, mostly amphibolite, of the Sargur series (SHADAKSHARA SWAMY et al., 1995). The gneiss is composed of quartz, oligoclase, sericite, biotite and chlorite minerals. Accessory minerals include apatite, epidote, allanite, titanite, ilmenite and zircon. Biotite crystals are often chloritized and oligoclase crystals are frequently sericitized (BRAUN et al., 2009). The average thickness of the immature saprolite is, at the watershed scale, 15 meters. It has been shown that, in the saprolite, the weathering sequence is biotite ≈ chlorite > plagioclase >> quartz ≈ sericite (BRAUN et al., 2009). The soil cover is mainly composed of a red soil-black soil system (BARBIERO et al., 2007; IUSS-WORKING-

GROUP-WRB, 2006). Shallow red soils (Ferralsols and Chromic Luvisols) from 1 to 2 meters in depth dominate (see soil map of Mule Hole in (BARBIERO et al., 2007)). Lithogenic quartz, sericite and, to a lesser extent, plagioclase are preserved within the solum. The lower part of the hill slope and flat valley bottoms are covered with, on average, 2 m of black soils (Vertisols and Vertic intergrades). The other occurrence of the black soil is lithodependant with development of deeper soils (2.5 m) on amphibolite-rich bedrock located in the depressions on the crest line. The black soils are dark-coloured with shrink-swell potential. At Mule Hole, the red soils cover 66% of the whole watershed area, the black soils 12% and the saprolite outcrops 22%.

At Maddur and Mule Hole, the main visible reservoir for the pedogenic carbonates is the B horizon of black soils from flat valley floors and crest lines. The pedogenic carbonates appear disseminated in the black soil matrices either as loose, irregular and friable nodules of millimetric size or as indurated botryoidal nodules of centimetric to pluricentimetric size. The loose nodules are preferentially located in the upper part of the B horizon and are interpreted as orthic nodules, with skeleton grains similar to the surrounding soil and having a gradual transition to the soil matrix, attesting to their *in situ* formation (WIEDER and YAALON, 1974; WIEDER and YAALON, 1982). The indurated botryoidal nodules consist of dense, hard calcite nodules with sharp margin akin to those described in other Indian vertisols (SRIVASTAVA et al., 2002). They extend from the surface within the erosion zones to about two meters in depth. Most of them display a septaria system leading sometimes to hollows. Their sharp boundaries with the soil matrices indicate that they have been subjected to pedoturbation. However, the skeleton grains are similar to those of the

soil matrix. They are considered as disorthic nodules (WIEDER and YAALON, 1974). The pedogenic carbonates also occur at the top layers of the saprolite within both watersheds either as disseminated pluricentimetric indurated nodules or carbonate-cemented lumps of centimetric to decimetric size. Both occurrences are rich in residual gneissic primary minerals. Detrital indurated botryoidal nodules are found in abundance in the sandy sediments of the streambeds. They display significant dissolution features and may derive from the indurated pluricentimetric nodules from black soils.

4 Sampling and analytical procedures

4.1 Sampling of pedogenic carbonates and black soil matrices

The pedogenic carbonate sampling is based on previous pedological studies carried out within both Mule Hole and Maddur watersheds (BARBIÉRO et al., 2010; BARBIÉRO et al., 2007). Two soil sequences and an erosion spoon at Mule Hole (Figure 2) and one soil sequence at Maddur (Figure 3) were selected for specific sampling. The loose millimetric nodules were sampled between the ground surface and a depth of 200 cm in the black soil profiles from the valleys. They come from soil catena, namely T1 (MHK-1, MHK-2) and T2 (MHH-1, MHH-2) at Mule Hole (Figure 2A and 2B) and T3 at Maddur (MAN-1) (Figure 3), respectively. The indurated botryoidal nodules from black soils were sampled (i) within the profiles MHT-1 and MHT-2 and at the surface (MHK-3) of the T1 soil catena (Figure 2A) and (ii) in eroding brook banks at Maddur (MAST). Indurated botryoidal nodules from saprolite were collected within an erosion spoon in upslope position (MHS-1, Figure 2C). The lumps of carbonate-cemented saprolite were collected at Maddur at a depth of 300 cm (MAS-1, MAS-2) (Figure 3).

In order to better infer the link between carbonate nodules and the black soil matrices, a small pit, namely MHT-2, was dug in the middle of the poorly drained plain in continuation with the T1 catena at Mule Hole. This portion of land is mainly covered by tufted grasses and rare trees (*Ceriscoides turgida, Diopyrs melanoxylon and Emblica officinalis.*). There is no litter on the ground except under trees. On the day of sampling (12/05/2008) the ground surface showed a large crack network. From the ground surface to a depth of 220 cm, the solum, developed on gneiss, shows the succession of the following horizons with diffuse boundaries (Figure 2A):

- The horizon A1, developed from the ground surface to 20 cm, has a dark brown colour (7.5YR2.5/1), a granular to a fine sub-angular blocky structure and a fine loamy texture. Grass roots are very abundant.
- The A2 horizon, from 20 to 50 cm, progressively changes downward from fine blocky to prismatic while the texture becomes more clayey.
- In the horizon Bkss, from 50 to 170 cm, the structure is massive and prismatic, the texture clayey and the colour dark grey (10YR3/1). Slickensides are abundant. The first pedogenic carbonates occur in this horizon at 50 cm. They are indurated and millimetric at the top of the horizon and increase in size up to several centimetres downwards. They are sometimes broken. The soil matrix is not effervescent to dilute HCl. Some saprolite pebbles are present.
- In the horizon BCk, from 170 to 220 cm, the structure is prismatic, the texture fine loamy and the colour yellowish (2.5Y3/1), some scarce indurated nodules are present at 190 cm.

In the whole profile, Fe-oxides occur as coatings on coarse quartz grains as well as impregnating matrix cements and Fe-Mn globules. These Fe-Mn cements depict redoximorphic features. Matrix samples devoid of visible pedogenic carbonates were

collected every 20 cm from the surface to a depth of 220 cm.

4.2 Morphology and mineralogy

Thin sections were prepared from pedogenic carbonates after impregnation with epoxy resin. The investigations were carried out with (i) optical polarizing microscope equipped with cathodoluminescence at G2R (Géologie et Gestion des Ressources Minérales et Energétiques, Nancy) and (ii) scanning electron microscope equipped with back scattered electron (BSE) and energy dispersive spectrum (EDS, Jeol 6360LV) at LMTG (Laboratoire des Mécanismes de Transfert en Géologie, Toulouse). The mineralogical composition of the bulk materials (randomly oriented samples) was determined by powder X-ray diffraction. Patterns were collected with a CPS 120 Inel curve detector (λ CoKα1 = 1.78897 Å). The following conditions were used for the X-Ray analyses: Voltage - 40 kV, current - 25 mA, scan range between 0.295° and 107.247° 2Θ, step size - 0.029° and total counting time - 1200 s. The mineralogy of separated clay fractions was also determined by X-ray diffraction analysis for three different samples with oriented mounting: A sample that was air-dried, a sample treated with ethylene glycol and a sample heated at 490 °C. The analyses were performed with a G3000 Inel goniometer (λ CuKα1 = 1.5418 Å), with a Si diode as detector. The following conditions were used for the X-Ray analyses: Voltage - 30 kV, current - 40 mA; scan range between 2.3° and 34.61° 2Θ and counting time of 2s per step interval of 0.03° 2Θ.

Bulk densities (ρ) were determined by the paraffin method with a Sartorius® density kit (10 replicates) for soil samples and indurated nodules.

4.3 Elemental composition and Sr isotope analyses

For subsequent investigations, the pedogenic carbonates were manually separated from the soil matrix using tweezers, washed with ultrapure milliQ® water and dried at 50°C. Sub-samples were powdered in an agate mortar.

The recovery of the carbonate fraction in solution is based on the methods described in (HAMIDI et al., 2001) and (CHIQUET et al., 1999): 150 mg of powdered nodule were leached with Suprapur 0.25N HCl in centrifuge tubes. The residual fraction was separated from the carbonate soluble fraction by centrifugation at 4000 rpm. Several successive acid leaching steps were carried out to recover the maximum of the carbonate fraction. The residual fraction was rinsed with ultrapure milliQ® water and then dried. The mass fraction of carbonate for each sample was calculated by difference between the initial sample and dried residue weights. The residual fraction was then digested with HF-HNO_3. Both carbonate and residue solutions were evaporated and recovered with 15N HNO_3.

The solutions were analyzed for major elements with a ICP-AES (Iris Intrepid III, Ecole Nationale Supérieure Agronomique, Toulouse) with a mean uncertainty of 10% and for trace elements with a ICP-MS (Perkin Elmer Elan 6000, LMTG Toulouse) with a mean uncertainty better than 10%.

For the Sr isotopic analyses, an aliquot containing at least 500 ng of Sr was passed through a Sr-Spec TM column (DENIEL and PIN, 2001) with a chromatographic extraction automat developed at the LMTG. $^{87}Sr/^{86}Sr$ isotopic ratios were measured on a TIMS Finnigan Mat 251 at LMTG Toulouse and VG Sector at Strasbourg using a semi-dynamic collection and yielding an uncertainty better than 0.00001 (2σ). The accuracy was controlled by regular measurements of the NBS 987 standard. The mean value of 4 measurements of NBS 987 performed during the course of this study at Toulouse is $0.710246 \pm 12 \quad 10^{-6}$ (2 σ).

Black soil samples were dried and sieved. Bulk soil chemical analyses were carried out at the SARM (Centre de Recherche Pétrographique et Géochimique-CNRS, Vandoeuvre-lès-Nancy). After $LiBO_2$ fusion and HNO_3 acid digestion, Si, Al, Fe, Mn, Mg, Ca, Na, K and Ti were analyzed by ICP-AES and Sr, V, Cr, Rb, Ba, Pb, Zr, Th, U, Y and REE by ICP-MS. For most of the elements, the results show an uncertainty better than 5%. It is better than 10%

for Mn, Rb, Zr, U, Th and Tm and better than 15% for Ho. Soil pH (both pH_{water} and pH_{KCl}) was measured on a 1:3 solid:liquid mixture with deionised water and 1N KCl, respectively. Exchangeable cations were measured with the cobaltihexammine chloride method (Laboratoire de Sols INRA, Arras, France). The partial pressure of CO_2 in both black and red soil profiles was measured with an analyser LFG20 (ADC) in 2004.

4.4 U-Th series isotope analyses

U-Th analyses were performed on four occurrences at Mule Hole (MHH-1c, MHH-1d, MHS, MHT-1) and four at Maddur (MAST, MAN, MAS1, MAS2), with duplicates on MHH-1c, MHH-1d, MHS and MAST. Non-broken, individual pluricentimetric nodules and lump blocks were initially selected to perform the analyses. However, on account of their small size, several loose nodules were combined for analysis.

The carbonate nodules were handled following the procedure for dirty carbonates (BISCHOFF and FITZPATRICK, 1991) based on full digestion of 5 selected sub-samples. After addition of ^{229}Th and ^{236}U spikes the carbonate fraction was dissolved with bi-distilled HNO_3, the residue digested separately with HF-HNO_3 and evaporated. The digested residue was dissolved in bi-distilled HNO_3 and mixed up with dissolved carbonate fraction for complete homogenization of the sub-sample.

U and Th were separated and purified by ion exchange chromatography using AG1 X8 resin (CHABAUX et al., 2003; DEQUINCEY et al., 2006). Procedure blanks are < 1pg and ~10 pg for U and Th, respectively, which is negligible compared to the U and Th amounts in samples, typically ranging from 10 to 20 ng. U isotopic composition was determined on a MC-ICP-MS Finnigan Mat Netpune using a multi-static collection mode, optimized for measurements of samples with highly variable U concentrations. Precise isotopic measurements can be obtained with either internal or external normalization. Typical uncertainty for 10 ng of NBS 960 standard measurement is 5‰ and 1‰ on $^{234}U/^{236}U$ and $^{236}U/^{238}U$, respectively (internal

304 error). Thorium isotopic ratios were also measured in multi-static collection mode. External
305 normalization was used for $^{230}Th/^{229}Th$ and $^{232}Th/^{229}Th$ ratios calculation. Internal error for
306 10ng of IRMM 035 standard measurement is 1.5‰ and 4‰ on $^{230}Th/^{229}Th$ and $^{232}Th/^{229}Th$,
307 respectively. The external uncertainties of $^{230}Th/^{238}U$, $^{234}U/^{238}U$, $^{232}Th/^{238}U$ for samples take
308 into account the uncertainties on the sample and standard measurement as well as the
309 uncertainty on the spike concentration.

310 Isochron ages were calculated using the ISOPLOT 3.00 program (LUDWIG, 2003).
311 Isoplot corrects samples for detrital contamination (^{232}Th) based on 3D diagrams of $^{232}Th/^{238}U$
312 - $^{230}Th/^{238}U$ – $^{234}U/^{238}U$ activity ratios, further indicated in brackets. The intercept of the best-
313 fit isochron is used to determine the authigenic ($^{234}U/^{238}U$) and ($^{230}Th/^{238}U$) composition
314 required for age calculation. It calculates: (1) the age of the sample and the uncertainties
315 associated with each age as well as (2) the Mean Square of Weighted Deviates (MSWD) and
316 the probability of fit statistics.

317 # 5 Results

318 The vertical distributions of major oxides, selected trace elements, bulk densities and
319 grain size fractions for the black soil matrices of the profile MHT-2 are listed in Table 1. The
320 concentrations of major and trace elements along with the $^{87}Sr/^{86}Sr$ isotopic ratios for the
321 labile and residual fractions of the pedogenic carbonates and the parental gneiss are reported
322 in Table 2. Elemental ratios such as Ce/Ce* and $(La/Sm)_N$ are also mentioned. The
323 concentrations of major elements and strontium along with the $^{87}Sr/^{86}Sr$ isotopic ratios of
324 rainwater samples are presented in Table 3. The U-Th series dating of pedogenic carbonates
325 are reported in Table 4.

326 ## 5.1 Mineralogy and element behaviour in the black soil profile MHT-2

327 XRD analyses of samples from the black soil profile MHT-2 indicate that the residual

328 mineral fractions are dominated by quartz and oligoclase with traces of sericite. In the clay
329 size fractions, smectite dominates with kaolinite. The oxyhydroxide phases include ferric
330 compounds such as ferrihydrite, maghemite and lepidocrocite.

331 Grain-size distribution, CEC and both pH_{water} and pH_{KCl} data are portrayed as vertical
332 profiles for the black soil samples in Figure 4. The bulk density increases with depth from 1.5
333 g/cm^3 in the first 20 cm to 2.0 g/cm^3 at 60 cm. This shift is accompanied with an enhancement
334 in the clay concentration from 200 to 400 g/kg. The grain-size fraction profile shows a net
335 decrease in fine sands, a moderate decrease in coarse and fine loam, a slight increase in coarse
336 sand and a net increase in clay. The pH_{water} of the soil matrix indicates that the soil is slightly
337 acidic to neutral between the ground surface and 100 cm with increasing values from 6 to 7.
338 After 100 cm depth, the pH value shifts to 8. pH_{KCl} is one unit less than pH_{water}. The CEC is
339 dominated by Ca^{2+}, which represents 58% (up to 17.2 cmol/kg) of the exchangeable cation
340 pool between 0 and 100 cm and 53% (up to 21.2 cmol.kg) between 100 and 220 cm,
341 respectively.

342 A correlation analysis including both physical properties and elemental composition
343 shows that positive correlations, with coefficient $r^2 \geq 0.7$ (n = 14), exist between (i) the clay
344 content and Al, Rb, Fe, Ti, Mg and K, (ii) Al and V, Th, LREE-Ce and HREE, (iii) Y and
345 both LREE-Ce and HREE, (iv) Cr and Y and HREE, and (v) Ti and LREE-Ce and HREE.
346 Mn, Ce and Ba are positively correlated but heterogeneously distributed within the profile
347 with specific accumulation zones in the Bkss and BCk horizons at 60-80 and 160-180 cm
348 depth, respectively. On average Ce is depleted with Ce/Ce* ranging between 0.7 and 1.6. Na,
349 Sr, Si and, to a lesser extent, Ca are correlated with both sand and loam contents and anti-
350 correlated with the clay fraction-related cations. This indicates that these elements are mostly
351 controlled by residual plagioclase. This observation is supported by the positive correlation
352 between the Eu-anomaly (Eu/Eu*) and both Na and Si. Zr, controlled by residual zircon

crystals, is also strongly correlated with both the sand and loam contents. Strong negative correlation also exists between Th and Zr. U is slightly correlated with Th and both elements are concentrated between 140 and 160 cm depth.

5.2 Morphology and mineralogy of pedogenic carbonates

Figure 5 shows the indurated and saprolite nodules sampled in the black soils and their location in soil profiles. Figures 6, 7 and 8 portray the thin section microphotographs of indurated and loose nodules. The micro- to nano-porous matrix of both indurated and loose nodules is composed of a mixture dominated by brown micrite, phyllosilicate clay minerals and oxy-hydroxides (Figures 6 and 7). Abundant gneissic residual primary minerals are present in the nodules. Among them, quartz crystals dominate with lesser amount of plagioclase, epidote and zircon crystals. Quartz and plagioclase crystals are often epigenized by calcite (Figure 6G and 6H). Oligoclase and epidote crystals exhibit weathering features. A thin spathic sparite coating from 50 to 100 µm width wraps the outer shell of the indurated nodules (Figure 6F). This coating has not been observed in loose nodules (Figure 7A and 7B). The indurated nodules, sometimes hollow, display abundant large cracks partly filled up with sparite ranging from 20 to 300 µm width (Figure 6A to 6E). The primary mineral grains, especially quartz, are embedded with sparite coating varying from 10 to 100 µm thick (Figure 6E and 6F). Cathodoluminescence imaging indicates multiple growing steps for the micritic matrix of one sample, but zoning of fissure fillings is common to many nodules (Figure 6B and 6D). Various oxides of redox-sensitive elements such as Fe, Mn, V, Cr and Ce are concentrated along the outer shell of the indurated nodules (Figure 8A to 8D). These impregnations fill the microfissure network across the sparite domains and around the residual primary grains.

5.3 Elemental enrichment and depletion in the labile and residual fractions of pedogenic carbonates

The proportion of the labile fraction with respect to the residual fraction (i. e. detrital and non-carbonate authigenic material) in the pedogenic carbonates varies from 56 to 86 wt%. For a chemical element X, the normalization to the gneissic parent rock is defined by the ratio $\chi = [X]_{carbonate}/[X]_{average\ gneiss}$, with enrichment when $\chi > 1$ and depletion when $\chi < 1$. On average, the labile fraction is enriched compared to the parental gneiss in LREE (except Ce), HREE, Y, U and Sr (**Figure 9A and 9B**).

In labile carbonate fractions, the elemental enrichments are significantly higher within the loose nodules. The carbonate-cemented lump (MAS-1) shows a significant depletion in Sr ($\chi = 0.5$) and U ($\chi = 0.2$) while the enrichments in REE and Y remain moderate. For the other nodules, the χ sequence (minimum and maximum values within brackets) is: $\chi_{LREE\text{-}Ce}$ (1.8-15.9) > χ_U (1.0-9.5) > χ_Y (1.9-8.1) > χ_{HREE} (1.0-5.7) > χ_{Sr} (0.8-3.7). The individual REE χ values decrease from La ($2 \leq \chi_{La} \leq 20$) to Lu ($0.7 \leq \chi_{Lu} \leq 3.1$). Ce is mainly depleted ($0.1 \leq \chi_{Ce} \leq 3.9$) with only two χ values > 1 and negative Ce-anomalies (Ce/Ce*) between 0.02 and 0.44. In all nodules, the Mg, Mn, Ba contents display a slight depletion with average χ of 0.8. The Al, Na, Ti, Cr, Rb and Th contents are strongly depleted with average χ ranging between 0.01 and 0.1. The K, Ti and Zr contents, highly depleted, are below the detection limit.

The residual fractions are enriched in Mn, V, Cr and Ba (**Figure** 9C and D) with the following average χ sequence: χ_{Mn} (7.5) > $\chi_V = \chi_{Cr}$ (1.6) > χ_{Ba} (1.2) and significantly depleted in Al, K, Mg, Na, Sr, Fe, Rb, Th, LREE-Ce, HREE and Y with the average χ sequence: χ_{Fe} (0.8) > χ_{Th} (0.7) > χ_{Al} (0.6) ≈ χ_{Rb} (0.6) > $\chi_{LREE\text{-}Ce}$ (0.5) > χ_Y (0.4) ≈ χ_{Sr} (0.4) > χ_{HREE} (0.3) > $\chi_{Zr} \approx \chi_{Mg} \approx \chi_{Na} \approx \chi_K$ (0.2). Ca, Ti and U do not exhibit any fractionation. Ce is significantly fractionated compared to the other LREE with positive Ce-anomalies up to 2600.

5.4 $^{87}Sr/^{86}Sr$ isotopic signature for the solid material

The $^{87}Sr/^{86}Sr$ isotopic ratios of the labile fraction of the nodules vary from 0.712511 to 0.716661. In the residual fractions, the $^{87}Sr/^{86}Sr$ isotopic ratios are slightly more radiogenic than in the labile fraction and vary from 0.714743 to 0.726572. The Sr isotopic signatures of labile and residual fractions are correlated at the Mule Hole watershed scale. At a given location, however, the composition of the residual fraction is more heterogeneous than in the labile one. The analyses performed in the Maddur watershed (MAS, MAN) display a wide range of variation (0.716 to 0.726) in the residual fraction but a narrow range in the labile one (**Figure 10**). The Sr isotopic composition of the matrices of the nodule samples MHT-2a, b and c, representing the black soil signature, ranges from 0.717583 ± 10.10^{-6} to 0.717745 ± 13.10^{-6}. The Sr isotopic ratio measured in a bulk sample of Precambrian Peninsular gneiss from Mule Hole is 0.713174 ± 15.10^{-6}.

5.5 U-Th series of pedogenic carbonates

The results of U-Th analyses of carbonate sub-samples are displayed in Table 4, along with the calculated ages, uncertainties and MSWD provided by ISOPLOT 3.00 (LUDWIG, 2003). The comparison of the whole U concentrations with the ($^{234}U/^{238}U$) of the sub-samples defines two pedogenic carbonate populations according to the soil environment (Figure 11). Whatever the sampling site, the signature of the black soil carbonates corresponds to a range of concentration between 0.9 and 5.5 µg/g and ($^{234}U/^{238}U$) between 1.28 and 1.37. In the saprolite/red soil context, the U concentrations range from 0.3 to 1.5 µg/g and ($^{234}U/^{238}U$) between 1.10 and 1.25.

Calculated U-Th ages of loose carbonate nodules of Mule Hole are 2 ± 2 kyr (MSWD = 26) and 5.2 ± 4.8 kyr (MSWD = 14) for MHH-1c and 1.33 ± 0.84 kyr (MSWD = 0.73) and -0.8 ± 2 kyr (MSWD = 2.7) for MHH-1d. The age for the Maddur black soil loose carbonate nodule is 7.5 ± 2.7 kyr (MSWD = 2). Computation of the four indurated botryoidal nodule

425 samples from the Mule Hole and Maddur soil profiles, as well as the replicate of Mule Hole
426 saprolite, displays close ages, from 15.7 ± 4.8 kyr (MSWD =1.5) for MHT-1 to 21.9 ± 8.0 kyr
427 for MAST (MSWD =3.1). Finally, the ages of the larger indurated nodules at Maddur are 66
428 ± 65 kyr (MSWD =15) for MAS-1 and 60 ± 53 kyr (MSWD =3.5) for MAS-2.

429 # 6 Discussion

430 The combined isotopic, geochemical and mineralogical analyses of the different kinds
431 of carbonates and of black soil profile matrix derived from gneiss provide information about
432 the conditions of formation and accumulation of pedogenic carbonate in the solum. As
433 mentioned, the current MAR in the sub-humid zone of the climatic gradient is 900 to 1200
434 mm/yr, which is significantly higher than the range favourable for accumulation of carbonates
435 in the soil (50 to 700 mm/yr). The nodules and lumps found in the Mule Hole and Maddur
436 watersheds are therefore considered herein to be pedorelicts formed during conditions drier
437 than today. In the ensuing sections, the elemental translocations in the black soil matrices will
438 be first discussed followed by an assessment of the weathering conditions pertaining to the
439 precipitation of the carbonate pedorelicts with respect to the co-accumulated elements such as
440 U, Sr, REEs and Y. Subsequently, the origin of Ca in the pedogenic carbonates will be
441 inferred and the conditions of formation and preservation of carbonates according to the
442 climate and pedological contexts will be discussed.

443 ## 6.1 Elemental translocations in the Mule Hole regolith

444 A conventional method to infer the elemental translocations within regolith is to apply
445 a mass balance calculation based on the principle of mass conservation (BRIMHALL et al.,
446 1991; OH and RICHTER, 2005). For a chemical element j:

447 $$\frac{V_w \rho_w C_{j,w}}{100} = \frac{V_p \rho_p C_{j,p}}{100} + m_{j,flux} \quad (1)$$

448 Where the subscripts p and w refer to the parent and weathered materials, respectively.

449 V is volume in cm^3, ρ is bulk density in g/cm^3 and C_j is chemical concentration of any
450 element j in weight percent (wt%). The $m_{j,flux}$ represents the mass of an element j moving into
451 or out of the system. The $m_{j,flux}$ is positive if the element j is accumulating in the system and
452 negative if j is leaching from the system.

453 The volumetric strain (ε) or volume change is calculated from the density ratios ρ and
454 conservative element concentrations C_i in the regolith by:

455 $$\varepsilon_{i,w} = \frac{\rho_p . C_{i,p}}{\rho_w . C_{i,w}} - 1 \qquad (2)$$

456 Positive values of $\varepsilon_{i,w}$ indicate expansion, negative ones indicate collapse and values
457 around zero, isovolumetric weathering.

458 The addition or subtraction of a chemical element j, either by solute migration or
459 mechanical translocation, is quantified by the open-system mass fraction transport function
460 ($\tau_{j,w}$) :

461 $$\tau_{j,w} = \left(\frac{\rho_w . C_{j,w}}{\rho_p . C_{j,p}} \right) . (\varepsilon_{i,w} + 1) - 1 \qquad (3)$$

462 Because the calculation of $\tau_{j,w}$ takes into account both residual enrichment and
463 deformation, a positive value for $\tau_{j,w}$ reflects a true mass gain in element j of the weathered
464 rock compared to the parent rock and a negative value indicates a mass loss. If $\tau_{j,w} = 0$, the
465 element is immobile during weathering with respect to the volume of regolith considered.

466 In a recent companion paper, combined geochemical, mineralogical and geophysical
467 investigations were used to attempt a mass balance reconstruction at the Mule Hole watershed
468 scale (BRAUN et al., 2009). Titanium was used as an immobile element in the τ calculation for
469 bulk samples of the gneiss-derived saprolite and the red soil. This previous work did not take
470 into consideration the less abundant black soil areas (12% of the whole watershed), which
471 could be, along with saprolite, the major reservoirs for the storage of pedogenic carbonates at

472 the watershed scale. In the present study, the mass balance calculation has been performed on
473 the black soil matrices primarily to consider the elemental translocation trends that have
474 occurred in the solum. The variation of $\varepsilon_{Ti,w}$ as a function of depth indicates that there is a
475 dilation from 10 to 50% in the upper 40 cm certainly due to both root action and possible
476 translocation of Ti-bearing particles with the clay size fraction emphasized by the good
477 correlation between Ti concentrations and the clay fraction. From 40 to 220 cm depth the
478 lower part of the profile experienced a negative strain leading to a net loss of volume, i.e.
479 collapse of about 20%. Except for Cr and V, which are accumulated in the solum, all other
480 elements analyzed are depleted with the following average τ sequence in the black soil
481 matrices: Na ≈ K (80%) > Mg ≈ Ba ≈ Ce ≈ LREE-Ce (60%) > HREE ≈ Rb ≈ Th ≈ Y (50%) >
482 Al ≈ Si ≈ Ca (40%) > Zr (30%) > Fe (20%) > Mn ≈ U (10%). Both depth-τ relationships
483 (Figure 12) and the correlation analysis facilitate the categorization of the elements into four
484 groups, depending on their relative mobility and geochemical reactivity (DRIESE et al., 2000;
485 STILES et al., 2001; STILES et al., 2003).

486 • The first category includes the elements linked to the primary framework minerals, i.e.
487 the residual minerals (Figure 12F). Elements such as Ca, Na, Sr, Si, Zr are correlated to
488 the sand and loam fraction attesting to the preservation of quartz, zircon, and plagioclase
489 in the solum,

490 • The second group is related to the elements linked to clay concentration and includes K,
491 Rb, Al, Ti, Mg, and, to a lesser extent, REE and Y (Figure 12C),

492 • The third group is composed of the redox-responsive elements, Fe, Mn, Ce, Cr and V
493 (Figure 12E). The transport functions are complex for Mn and Ce suggesting
494 redistribution processes in the soil profile with zones of dissolution and accumulation.
495 The similar transport functions for Mn and Ba suggest the presence Mn-Ba oxides as
496 psilomelane $[Ba(Mn^{2+})(Mn^{4+})_8O_{16}(OH)_4]$ or todorokite

497 [(Mn,Mg,Ca,Ba,K,Na)$_2$Mn$_3$O$_{12}$·3H$_2$O] in the solum. Ce-oxide (cerianite) can be
498 associated with the presence of these phases. Cr and V are positively correlated and are
499 known to be associated with iron oxides and oxyhydroxides as chromate and vanadate,
500 • The fourth group includes U and Th, for which a dual control does certainly exist by
501 both residual minerals and clays (**Figure 12**D). For instance U can be in zircon. The
502 transport functions for U and Th show a similar shape with however a higher depletion
503 in Th.

504 In summary, the solum is characterized by the leaching of trace elements such as REE,
505 Y, U and Th and a strong redistribution of the redox sensitive elements (Fe, Mn, Cr, V, Ce),
506 compared to the chemistry of the pedogenic labile carbonate fraction which shows selective
507 accumulation of Sr, U and ∑LREE-Ce.

508 ### 6.2 Sources of Ca in the pedogenic carbonates

509 Because of the similar chemical behaviour of Sr and Ca, the Sr isotopic composition is
510 often considered as a proxy to identify the Ca origin in pedogenic carbonates (CAPO and
511 CHADWICK, 1999; CAPO et al., 1998; CHIQUET et al., 1999; DART et al., 2007; HAMIDI et al.,
512 2001). The Sr isotopic composition, which is a conservative tracer, reflects the sources of Sr
513 available in the soil environment. In the soil solution, the Sr content depends on the mixing of
514 both atmospheric and *in situ* weathering sources. Attempting to quantify the Ca contribution
515 of each source within the labile fraction of the pedogenic nodules will therefore depend on
516 both the Sr isotopic signature and the Sr/Ca molar ratio of each end-member. The proportion
517 of Ca from the atmospheric source ($\%Ca_{atm}$) in the labile fraction is given by the following
518 formula (CAPO et al., 1998):

519 $$\%Ca_{atm} = \frac{\left(\left(^{87}Sr/^{86}Sr\right)_{mix} - \left(^{87}Sr/^{86}Sr\right)_{isw}\right)K_{isw}}{\left(\left(^{87}Sr/^{86}Sr\right)_{mix} - \left(^{87}Sr/^{86}Sr\right)_{isw}\right)K_{isw} + \left(\left(^{87}Sr/^{86}Sr\right)_{atm} - \left(^{87}Sr/^{86}Sr\right)_{mix}\right)K_{atm}} \quad (4)$$

520 Where K_{atm} and K_{isw} are the Sr/Ca molar ratios for the atmospheric and the *in situ*

521 weathering sources, respectively. $(^{87}Sr/^{86}Sr)_{mix}, (^{87}Sr/^{86}Sr)_{atm}, (^{87}Sr/^{86}Sr)_{isw}$ are the Sr isotopic
522 ratios for the labile carbonate fraction, the atmospheric end-member and the *in situ*
523 weathering end-member, respectively. The composition of both end-members is discussed
524 below.

525 The $^{87}Sr/^{86}Sr$ isotopic ratio of rainfall at Mule Hole ranges between 0.708751 and
526 0.718439 (Table 3), which is more extended than the carbonate phase signature. However, the
527 most radiogenic rains are characterized by high K/Cl ratios. Although the rain collectors are
528 located in an open area, some rain events, i. e. monsoon storms, can be significantly
529 influenced by emissions from the local vegetation. This affects the $^{87}Sr/^{86}Sr$ rain signature
530 towards more radiogenic values. For this reason, the most likely atmospheric source should be
531 represented by the sample with the lowest K/Cl ratio, which has a $^{87}Sr/^{86}Sr$ ratio of 0.708751.
532 This value, even if slightly lower than the seawater isotopic ratio, is consistent with the
533 observations that the SW monsoon has a dominant marine component at the sub-continent
534 scale (SIVA SOUMYA et al., 2009).

535 The Precambrian Peninsular gneiss of the Gundlupet area also displays a wide range
536 of Sr isotopic signatures, from 0.713174 to 0.783180 (JANARDHAN and VIDAL, 1982) and this
537 study, Table 1). Since the variation of the Sr isotope ratios is mineralogically controlled, the
538 whole rock isotopic ratio varies according to the relative abundance of (i) less radiogenic
539 minerals, such as plagioclase and apatite with $^{87}Sr/^{86}Sr$ close to 0.7 and (ii) the most
540 radiogenic minerals such as biotite, with $^{87}Sr/^{86}Sr$ from 0.9 to 4.3 (MEISSNER et al., 2002).
541 Moreover the weathering sequence should also have a significant impact on the local
542 variation of the Sr isotopic ratios in the regolith (PETT-RIDGE et al., 2008). Therefore taking
543 an average $^{87}Sr/^{86}Sr$ signature for the parent rock as the *in situ* weathering end-member is not
544 pertinent. Another alternative is to consider that the $^{87}Sr/^{86}Sr$ signatures of the residual
545 fraction of the pedogenic carbonates represents the weathered material present when the

546 carbonate phase was formed. This is consistent with (1) the trend observed between the
547 $^{87}Sr/^{86}Sr$ signatures of labile carbonate fractions and the $^{87}Sr/^{86}Sr$ signatures of the
548 corresponding residual fractions, which means that each carbonate fraction is at least partly
549 linked to the local soil composition (**Figure 10**) and (2) the similarity between the $^{87}Sr/^{86}Sr$
550 signatures of black soil matrices of MHT2 a, b, c (from 0.717583 to 0.717745) and those of
551 the residues of the MHT2 carbonate nodules (from 0.717911 to 0.718295). The best local
552 $^{87}Sr/^{86}Sr$ signature of rock should thus be provided by the residual phase of each sampling
553 location for the gneiss-derived samples.

554 According to the compositions of the atmospheric and lithologic Ca sources discussed
555 above and based on equation 4, the calculated proportion of Ca derived from the lithologic
556 source varies from 24 to 82% for the loose nodules, from 37% to 75% for the indurated
557 botryoidal nodules and from 5 to 29% for the carbonate-cemented saprolite lumps. The
558 sample MAS-2 with the lowest proportion of lithologic derived Ca (5%) has the most
559 radiogenic signature in the residual fraction. It is out of the trend defined by the other samples
560 (Figure 10). For this particular sample, the residual fraction may not be representative of the
561 *in situ* weathering source, leading to an underestimation of the lithologic source contribution.
562 If this sample is set aside, the whole average contribution of the lithologic component is 55%
563 which is, on average, higher than that found in South Australia (< 2%-30%, DART et al., 2007;
564 LINTERN et al., 2006; QUADE et al., 1995), in Spain (3 – 33%, CHIQUET et al., 1999) and in
565 United States (2 - < 40%, (CAPO and CHADWICK, 1999; NAIMAN et al., 2000). However, two
566 studies reported, though not quantified, a preponderant contribution of *in situ* weathering (i)
567 in the Atacama Desert, Chile in relation with saline groundwater evaporation and eolian
568 redistribution (RECH et al., 2003) and (ii) in calcrete hardpans from South Peninsular India
569 (DURAND et al., 2006a; DURAND et al., 2006b).

570 The evolution of Sr isotopic signatures from seashore towards 100 to 200 km inland is

571 often interpreted as a result of the decreasing influence of sea salts (CAPO et al., 2000; DART
572 et al., 2007; QUADE et al., 1995; RECH et al., 2003; WHIPKEY et al., 2002). For pedogenic
573 carbonates beyond 200 km inland, the proportion of *in situ* weathering *versus* atmospheric
574 sources is still poorly understood. Nevertheless, from the available dataset, two populations of
575 pedogenic carbonates might be distinguished: The first with 0 to 15% of Ca lithologic source
576 located in desert regions with current MAR < 300 mm (CAPO and CHADWICK, 1999; CHIQUET
577 et al., 1999; DART et al., 2007; LINTERN et al., 2006), and the second with higher lithologic
578 contribution located in semi-arid regions with current MAR ranging between 400 and 700
579 mm (CHIQUET et al., 1999; DART et al., 2007; DURAND et al., 2006a; NAIMAN et al., 2000).
580 According to these studies, the Ca contribution of the *in situ* weathering might therefore be
581 dependent on MAR if we consider that the pedogenic carbonates formed in similar climatic
582 conditions to that prevalent today, which is a reasonable assumption. A significant release of
583 Ca from weathering indeed needs relatively humid conditions, which may limit the influence
584 of atmospheric inputs, especially dusts. If this trend is meaningful, it implies that the
585 pedogenic carbonate occurrences at Mule Hole and Maddur would have formed within MAR
586 range of 400 – 700 mm, which is 2-3 times less than the current MAR. This is realistic since
587 both watersheds are located in a position of the climatic gradient where large MAR variations
588 exist and have existed. At this stage, an important implication is that these pedogenic
589 carbonates constitute an efficient trap for atmospheric CO_2 consumed by silicate weathering
590 since their formation in semi-arid conditions.

591 **6.3 Controls on the trace-element chemistry of pedogenic carbonates**

592 The carbonates exhibit large variations respectively in U/Ca Sr/Ca, Ce/Ca, Mg/Ca
593 molar ratios, namely 27 fold (from 9.8 10^{-8} to 2.7 10^{-6}), 7 fold (from 1.5 10^{-4} to 9.8 10^{-4}),
594 30 fold (from 5 10^{-6} to 1.6 10^{-4}) and 7 fold (from 1.3 10^{-2} to 9.1 10^{-2}). Moreover, the
595 ($^{234}U/^{238}U$) signatures of sub-samples analysed for U-Th dating range from 1.115 to 1.374

596 (Figure 11). When compared to each other, the Sr/Ca, U/Ca, Mg/Ca molar ratios and
597 ($^{234}U/^{238}U$) signatures define trends with two populations according to the pedological
598 environment: the most U-, Sr- and Mg- concentrated carbonates, with highest ($^{234}U/^{238}U$)
599 signatures correspond to black soil occurrences, whereas the less U-, Sr- and Mg-
600 concentrated carbonates, with lowest ($^{234}U/^{238}U$) signatures, correspond to the saprolite ones.
601 This means that the carbonate composition would be controlled, on a first order, by the
602 physico-chemical properties of the host materials of the soil profile.

603 The high ($^{234}U/^{238}U$) values of black soil carbonates, from 1.27 to 1.374, indicate that
604 they formed in similar pedological conditions, whatever the location in the climatic gradient
605 (Maddur or Mule Hole), whatever the morphology of carbonates (loose or botryoidal) and
606 whatever the mean age of the occurrences (20 kyr or younger) (Figure 11). The high specific
607 area and the confinement of solutions due to the high clay content of black soils may be
608 responsible for the enhancement of α-recoil process in soil solutions and subsequent relative
609 enrichment of ^{234}U in pedogenic carbonates precipitated from the soil solutions.

610 There could be several factors for explaining the large variations in U, Sr and Mg
611 concentrations according to the pedological context. First, they could fortuitously result from
612 variations in the chemical composition of the local black soil and saprolite, themselves
613 dependant on the local bedrock composition. Such a hypothesis may be tested if one assumes
614 that the chemical signature of the residual fraction of each carbonate is representative of the
615 local soil/saprolite composition (see section 6.2). However, the U/Ca, Sr/Ca and Mg/Ca molar
616 ratios of the residual fractions of saprolite carbonates are undistinguishable from those of
617 black soil carbonates. Alternatively, the relationship between carbonate composition and
618 pedologic context could be indirect and result from variations in parameters known to control
619 the partition coefficients of U, Sr and Mg in calcite that forms in marine environments such as
620 temperature, crystal growth rate and/or the chemical composition of the soil solution (e.g. pH,

carbonate concentration). For instance, the incorporation of Mg into calcite mainly depends on temperature (e.g. GASCOYNE, 1983; HUANG and FAIRCHILD, 2001; RIMSTIDT et al., 1998; ROSENTHAL et al., 2007 and references therein), which makes the Mg/Ca ratio in plankton a proxy for reconstructing marine paleo-temperatures: the Mg/Ca ratio in foraminifers increases by 8-10% per °C (LEA et al., 1999). However, the incorporation of trace elements into calcite from marine organisms is often species dependent, making any extrapolation to soil processes equivocal. Experiments of inorganic and biogenic calcite growth indicate that at constant temperature, the strontium incorporation into calcite (D_{Sr}) is strongly correlated to calcite precipitation rate (R) (LORENS, 1981; NEHRKE et al., 2007; TANG et al., 2008; TESORIERO and PANKOW, 1996). For instance, (TANG et al., 2008) express this relationship at T = 25°C as $\log D_{Sr} = (0.214 \pm 0.026).\log R - 1.67 \pm 0.09$.

According to this relationship, a two-fold variation of D_{Sr}, which corresponds to the mean Sr variations between black soil carbonates and saprolite carbonates, would nearly correspond to a 25-fold variation in calcite growth rate. At T=5°C, the relationship between D_{Sr} and R is slightly different and a 2 fold variation of D_{Sr} would correspond to almost a 10 fold variation in the calcite growth rate (TANG et al., 2008). The influence of calcite growth rate on incorporation of Sr was proposed by (CHIQUET et al., 1999) for pedogenic carbonates in Spain and also invoked by (COLE et al., 2004) to account for high U and Sr concentrations in tufas, with in that case also include a possible effect of microbial mediation. If one considers that the growth rate of calcite is the preponderant mechanism for explaining the U and Sr contents in the Maddur and Mule Hole pedogenic carbonates, the experiments of (TANG et al., 2008) would indicate that the relative growth rates of the carbonate-cemented lumps could have been up to several orders of magnitude lower than for the nodules of the black soils. This may explain the difficulty in accurate U/Th dating of the carbonate-cemented lumps, which provided high MSWD and large age uncertainty. The correlation of Mg

concentration with U and Sr, despite Mg incorporation into calcite, is usually not related to the calcite growth rate (LOPEZ et al., 2009 and references therein), but could be explained by an additional temperature control (HUANG and FAIRCHILD, 2001), or by the presence in the soil of carboxyl-rich molecules that would enhance Mg incorporation (STEPHENSON et al., 2008). High Mg concentrations were indeed found in carbonate cements developed in organic rich environments by (MCCALL et al., 2001), who proposed that plant roots could be responsible for the Mg enrichments.

In which way the link between the carbonate growth rate and the nature of the pedologic context could be explained? According to (LOPEZ et al., 2009), who studied calcite precipitation in artificial seawater, 3-fold increase of CO_3^{2-} content in the water would be responsible for a more than 20-fold increase of the calcite crystal growth rate, which is on the same order as growth variations deduced from mean Sr contents in black soils and saprolite. (NEHRKE et al., 2007) also noticed that at constant saturation degree, the calcite growth rate would depend on the Ca^{2+}/CO_3^{2-} ratio in the solution and would be maximal when it is close to 1. The Ca^{2+}/CO_3^{2-} ratio of the soil solution at the time of pedogenic carbonate crystallization is impossible to estimate. However, the CO_2 partial pressure (pCO_2), measured in a black soil profile at Mule Hole (MHT-1) ranging from 0.82% at 20 cm to 0.10% at 220 cm, support the idea that the black soil pore water would contain appreciably more dissolved CO_3^{2-} than the saprolite pore water located below 220cm.

The systematic negative Ce-anomaly in the carbonate labile fractions indicate that, at the time of their formation, the percolating soil solutions were oxidizing and Ce formerly deposited in other places in the profile. Similarities can be put forward with the behaviour of REE in more acidic environments where secondary Al-phosphate precipitation controls the REE chemistry (BRAUN et al., 1998). In the present case it seems that carbonate controls the REE-Ce chemistry. After carbonate formation, there is evidence that the percolating soil

671 solutions infiltrated the peripheral crack network of the nodules, when it existed, and
672 precipitated Ce and other redox-sensitive elements such as Fe, Mn, Cr and V (Figure 8). The
673 presence of these elements in the nodules supposes that they were mobilized in more humid
674 conditions than those prevailing during initial carbonate crystallization. Fe requires
675 significantly lower pε to be mobilized than Mn and Ce (STILES et al., 2001). (TRIPATHI and
676 RAJAMANI, 2007a) propose that mobilization of Fe, Mn and Ce results from alternating
677 aridity/humid periods. The fact that these elements precipitate in the cracks of the nodules
678 may indicate that indurated pedogenic carbonates underwent at least one significant humid
679 period since their formation. In addition, the lack of correlation between U/Ca and Ce/Ca in
680 labile fractions of carbonates indicates that the U and Ce mobility are not linked: the U
681 trapped in carbonates may have remained immobile during the relative humid periods.

682 In summary, the Sr, U and Mg contents and the ($^{234}U/^{238}U$) activity ratio in labile
683 fraction of carbonates reflect the conditions of formation of carbonates, mainly driven by the
684 soil type. The carbonate growth of black soil carbonates appears to be much faster than those
685 in saprolite based on better confinement of solutions and possible higher dissolved carbonates
686 in the soil solution. Ce concentrations are mainly localised in the cracks of carbonates, which
687 is interpreted to be the result of a relative humid period after initial carbonate formation.

688 ### 6.4 Paleo-monsoonal significance of pedogenic carbonate occurrences
689 ### and influence on carbon storage

690 As discussed in section 6.2, carbonate accumulation in the Maddur and Mule Hole
691 watersheds probably occurred during climatic conditions drier than those of the present day,
692 i.e. with MAR ranging from 400 to 700mm; these results are important since relatively little
693 paleoclimate information is available in these cratonic regions. Out of the 12 dating attempts
694 performed on Mule Hole and Maddur carbonates, only seven provided ages with reasonable,
695 albeit not ideal, MSWD. Three attempts (MHH-1d(2), MHH-1c(1), MHH-1c(2)) failed

696 because the carbonates are too young to be dated by this U-Th method. The cemented
697 carbonate lumps from Maddur (MAS-1 and MAS-2) are probably the oldest occurrences but
698 their composition obviously does not result from a mixture between two simple end-members:
699 either these carbonates evolved as an open system, or their growth would have been rather
700 slow enough to encompass a wide range of ages in a single sample. This latter explanation
701 would be consistent with a slow growth of the carbonate (CHIQUET et al., 1999; TANG et al.,
702 2008) (see section 6.3). Consequently, the further discussion will focus on the significance of
703 the seven "successful" ages: (1) 1.33 ± 0.84 kyr (MHH-1d(1)), (2) 7.5 ± 2.7 kyr (MAN) and
704 (3) the group of 4 samples and one replicate with narrow age range from 15.7 ± 4.8 to
705 21.9 ± 8 kyr (MHT-1, MHS(1), MHS(2), MAST(1), MAST(2)).

706 The ages from (3) covers the Last Glacial Maximum, a period for which the SW
707 monsoon strength has been studied extensively through oceanic records in the Arabian Sea
708 (e.g. DUPLESSY, 1982; PRABHU et al., 2004; PRELL and VANCAMPO, 1986; ROSTEK et al.,
709 1993; SARKAR, 2000; VANCAMPO, 1986; VANCAMPO et al., 1982) and through continental
710 records in the Indian subcontinent (e.g. CANER and BOURGEON, 2001; RAJAGOPALAN et al.,
711 1997; SINGH et al., 1988; SUKUMAR et al., 1993). All the climate proxies used for these
712 previous studies, pollen distribution, $\delta^{18}O$ of foraminifers and $\delta^{13}C$ of organic matter support
713 a relatively weak SW monsoon at that time (Figure 13).

714 The closest oceanic records of monsoon strength since the Late Pleistocene are located
715 at 10°N and 15°N in the eastern Arabian sea (VANCAMPO, 1986). Based on two pollen records
716 of Rhizophora (Mangrove), (VANCAMPO, 1986) considered climate to have been very arid
717 between 18-22 kyr ago, but with persistence of low summer precipitation at 10°N which is
718 consistent with the formation conditions of the pedogenic carbonates from the climatic
719 gradient. The strength of SW monsoon and associated rainfall would have increased gradually
720 from 16.5 kyr BP and extended towards the North due to northward migration of the

721 Intertropical Convergence Zone (VANCAMPO, 1986). The maximum rainfall intensity,
722 corresponding to a maximum extension of the mangrove, was reached 11 kyr BP before a
723 decrease during the Holocene. In the sub-humid zone of the gradient, the dry conditions
724 prevailing at the LGM led to widespread occurrences of pedogenic carbonates in black soil
725 and saprolite, which are still preserved. No trace of pedogenic carbonates was found in the red
726 soil, which represents 80% of the soil cover in these watersheds. This may indicate that the
727 pedoclimatic conditions did not allow the carbonate occurrence, or that the carbonates were
728 dissolved during the maximum monsoon intensity that followed the LGM, between 15 and
729 5kyr, depending on studied locations and proxies (e.g. OVERPECK et al., 1996; RAJAGOPALAN
730 et al., 1997; RAMESH, 2001; VANCAMPO, 1986 and references therein). This long wet period
731 may have been responsible for Mn-Ce migration through the soil profile, as observed by
732 (TRIPATHI and RAJAMANI, 2007b), and for their precipitation in the cracks of nodules from
733 black soils and saprolite.

734 In South Peninsular India, fluctuations in Holocene monsoon intensity were recorded
735 in the Nilgiris Mountains, less than 100 km south from our study area. The studies were based
736 on $\delta^{13}C$ measurements in peat bogs (RAJAGOPALAN et al., 1997; SUKUMAR et al., 1993) and in
737 organic matter of andosols (CANER and BOURGEON, 2001). According to (SUKUMAR et al.,
738 1993) the regional climatic conditions changed from wet to arid between 10 and 6 kyr BP.
739 These arid conditions prevailed, with few low amplitude fluctuations, till the Medieval Warm
740 Period (ca. 0.5-0.7 kyr BP). This trend was confirmed by (RAJAGOPALAN et al., 1997) who
741 recorded a sharp wet peak at 9 kyr BP before an evolution towards arid conditions was
742 reached at 5 kyr BP and which was also maintained till the Medieval Warm Period. Both
743 youngest ages obtained from loose nodules in black soil of Mule Hole and Maddur,
744 1.33 ± 0.84 kyr (MHH-1) and 7.5 ± 2.7 kyr (MAN), respectively, fall within the arid period
745 detected from the continental proxies (RAJAGOPALAN et al., 1997; SUKUMAR et al., 1993)

746 (figure 13). The younger occurrence is also consistent with the arid climatic conditions found
747 in the sedimentary record of the inner shelf of Karwar, coastal Karnataka (CARATINI et al.,
748 1991).

749 Thus, it can be concluded that in semi-arid conditions (see section 6.2), black soils
750 favour carbonate production even during short dry periods. The fact that carbonate growth
751 rate is relatively high (see section 6.3) confirms this observation. Black soils would be
752 confined enough to also preserve several distinct generations of pedogenic carbonates, for
753 time spans exceeding those of dry periods. However, the maximum ages of carbonates seem
754 independent from the pedological context, but rather sensitive to the position in the climatic
755 gradient: from about 20 kyr for centrimetric nodules at Mule Hole (current MAR = 1100
756 mm/yr) to 200 kyr for the calcrete at Gundlupet (current MAR = 700 mm/yr, (DURAND et al.,
757 2007)). In between at Maddur (MAR = 900 mm/yr), the two occurrences are probably older
758 than the LGM. This would indicate that, rather than the pedologic context, the intensity of
759 rainfall during wet periods would play a role in the residence time of pedogenic carbonates.
760 Such control could occur in two ways: (1) the dissolution of carbonates due to increase of
761 water percolation through and leaching from the soil profile, or (2) physical removal due to
762 the erosion. The dissolution process would likely prevail in permeable media, such as shallow
763 saprolite: it could explain calcium accumulation in the deepest parts of the saprolite at Mule
764 Hole (BRAUN et al., 2009). Physical removal is currently observed at the outlet of the Mule
765 Hole and Maddur watersheds, where fragments of pedogenic carbonates are mingled with the
766 riverbed sandy sediments. The mean erosion rate calculated by (GUNNELL et al., 2007) with
767 ^{10}Be, 13.6 ± 2.9 mm/kyr, indicates that on average 1.4 m of soil cover would be removed in
768 100 kyr. This amount would be sufficient for explaining the absence of carbonate older than
769 20 kyr at Mule Hole, since older carbonate nodules would have been removed by erosion
770 processes.

7 Conclusions

A combination of mineralogical, geochemical and isotopic investigations has been carried out on the pedogenic carbonate nodules and black soil matrices of the sub-humid zone of the Western Ghâts rain shadow (South India) to understand the influence of climate and pedological conditions on the inorganic carbon storage in soils.

- The black soil matrices are characterized by the leaching of REE, Y, U and Th and a strong redistribution of the redox sensitive elements compared to the pedogenic carbonate chemistry which shows selective accumulation of Sr, U and ∑LREE-Ce,
- The proportion of Ca in the labile fraction of carbonates coming from the local silicate weathering was calculated using the $^{87}Sr/^{86}Sr$ ratio as a tracer of the Ca origin. The lithogenic component, assumed to be the residual phase of each carbonate, accounts for 24 to 82% of the Ca, with an average of 50%. This means that an equivalent part of the carbon trapped in these carbonates results from atmospheric CO_2 consumption by the local silicate weathering. The rainfall at the time of carbonate formation would have remained wet enough to allow silicate weathering and would correspond to semi-arid conditions, with MAR of 400-700mm/yr. This corresponds to 2-3 times less than the current MAR at Maddur and Mule Hole.
- The U, Sr, Mg contents and the ($^{234}U/^{238}U$) signature in the labile fraction of carbonates vary according to the pedological context, with high values in black soils and low ones in saprolite. They likely reflect the conditions of formation of carbonates: black soil carbonates would grow much faster than those from saprolite. Fast growth could due to a better confinement of pore waters that,

795 together with high clay content, enhance a-recoil processes and high
796 ($^{234}U/^{238}U$) signature. The presence of Ce, Mn and Fe oxides in the cracks of
797 carbonates indicate the occurrence of relative humid periods posterior to the
798 carbonate formation,

799 • The carbonate ages determined by the U-Th method range from 1.33 ± 0.84
800 kyr to 7.5 ± 2.7 kyr and to a cluster of five ages around 20 kyr, i.e. the Last
801 Glacial Maximum. These ages correspond to identified periods of weak SW
802 monsoon. The young occurrences are only located in the black soils that
803 therefore constitute a favourable environment for carbonate genesis and
804 subsequent atmospheric CO_2 storage in soils, even on short time scales.
805 However, the maximum age of carbonates rather depends on the location in the
806 climatic gradient than on the pedological context: at current MAR = 1100
807 mm/yr (Mule Hole) the older occurrence is around 20 kyr, whereas at MAR =
808 700 mm/yr calcretes are 200 kyr old (Gundlupet, DURAND et al., 2007). The
809 lifetime of pedogenic carbonates would be likely controlled by the intensity of
810 rainfall during wet periods and erosion processes.

8 Acknowledgments

The Kabini river basin is part of the ORE-BVET project (Observatoire de Recherche en Environnement – Bassin Versant Expérimentaux Tropicaux, www.orebvet.fr). Apart from the specific support from the French Institute of Research for Development (IRD), the Embassy of France in India and the Indian Institute of Science, our project benefited from funding from Université Paul Sabatier and INSU/CNRS (Institut National des Sciences de l'Univers / Centre National de la Recherche Scientifique) through the French programmes ECCO-PNRH (Ecosphère Continentale: Processus et Modélisation – Programme National Recherche Hydrologique), EC2CO (Ecosphère Continentale et Côtière) and ACI-Eau. It is also funded by the Indo-French programme IFCPAR (Indo-French Center for the Promotion of Advanced Research W-3000). The multidisciplinary research carried on the Mule Hole/Maddur watersheds began in 2002 under the control of the IFCWS (Indo-French Cell for Water Sciences), joint laboratory IISc/IRD. We thank the Karnataka Forest Department and the staff of the Bandipur National Park for all the facilities and support they provided. Ph. de Parseval (SEM, microprobe), M. Thibaut (XRD), J. Pironon (cathodoluminescence), F. Candaudap (ICP-MS), P. Brunet, F. Chabaux and T. Perrone (Sr isotopic ratios) are thanked for their assistance.

9 List of tables

Table 1: Major and selected trace elements of the black soil profile MHT-2.

<DL: Below detection limit; NA: Not Analyzed.

Table 2: Major, selected trace elements and Sr isotopic analyses of the pedogenic carbonates from the Mule Hole and Maddur watersheds.

<DL: Below detection limit; NA: Not Analyzed.

**(***) Obtained by weighing the residues

Table 3: Major, selected trace elements and Sr isotopic analyses of the rainwater samples. <DL: Below detection limit; NA: Not Analyzed.

Table 4: ^{238}U and ^{232}Th concentrations, ($^{232}Th/^{238}U$), ($^{230}Th/^{238}U$), ($^{234}U/^{238}U$) activity ratios and corresponding uncertainties in carbonate subsamples. The carbonate ages, their uncertainties and MSWD were calculated with Isoplot (LUDWIG, 2003).

10 List of figures

Figure 1: Climatic gradient of the Western Ghâts rain shadow, location of the Kabini river basin and the Mule Hole and Maddur experimental watersheds. The shaded area represents the boundaries of the sub-humid zone with the 900 mm/yr and 1500 mm/yr isohyets.

Figure 2: Location of carbonate nodules in selected soil catena from the Mule Hole watershed (BARBIERO et al., 2007, 2010). Pluricentimetric indurated nodules: MHT, MHS. Loose millimetric carbonates: MHK and MHH.

Figure 3: Location of carbonate nodules in the selected soil catena from the Maddur watershed. Cemented lumps from saprolite: MAS. Loose millimetric carbonates: MAN.

Figure 4: Vertical profiles of the grain-size distribution, CEC, pH_{water} and pH_{KCl} in the Mule Hole black soil MHT-2.

Figure 5: Macrophotographs of indurated nodules from soil catena of Figure 2. Catena A (MHT-1): (A) nodules in the black/red soil transition zone, (B) washed nodules and (C) broken nodule. Catena B (MHS): (D) erosion spoon where the saprolite nodules were sampled and (E) washed nodules. Cracks are filled with soil material.

Figure 6: Indurated nodule microphotographs with plain polarised light (A and C) and cathodoluminescence (B and D) photographs. Growing steps in micritic matrix (B) and in fissure fillings (D). E to H = back scattered electrons (BSE) photographs by SEM. (E) Filling of cracks with sparite. (F) Filling of crack and surface coating with sparite. (G) Weathered albite filled with sparite (H) Quartz cracks filled with sparite.

Sp : sparite. Mc : micrite. Q : quartz. SM : soil material. F : feldspar. Ox : oxides.

Figure 7: Loose nodule microphotographs (A) SEM-BSE microphotograph, (B) weathered plagioclase at the boundary between nodule and soil matrix.

Sp : sparite. Mc : micrite. Q : quartz.

Figure 8: Oxides in carbonate nodules SEM photographs (back scattered electrons). (A) Fissure filled by Mn oxides is cut cross by a crack. (B) On the left, Mn oxides border sparite. On the right, sparite cut cross Mn oxides. (C-D) Micritic matrix microporosity impregnated with Fe-oxides (C) and Ce-oxides (D).

Sp : sparite. Mc : micrite. Q : quartz. Ox : oxides. Fs : fissure. F : feldspar. Il : ilmenite.

Figure 9: Gneiss-normalized patterns for the labile carbonate fractions and the corresponding residual fractions: (A) loose nodules from black soil, (B) indurated nodules from black soil, (C) indurated nodules from saprolite and (D) carbonate-cemented lumps from saprolite.

Figure 10: Trend between the $^{87}Sr/^{86}Sr$ isotopic ratios in the labile fraction of carbonates and the $^{87}Sr/^{86}Sr$ of the corresponding residual fractions.

Figure 11: U concentrations versus ($^{234}U/^{238}U$) in the sub-samples of carbonates. Two pedogenic carbonate populations may be identified according to the soil environment, black soil or saprolite.

Figure 12: Vertical profiles of the density (A), strain (B) and the open-system mass fraction transport functions in the Mule Hole black soil for elements linked to clays and clay minerals (C, D), redox-sensitive elements and Ba (E) and elements mainly linked to the framework minerals (F).

Figure 13: Consistency of proxies for the Last Glacial Maximum weak monsoon and for more recent events. (A) Stratigraphy in Thar desert (JUYAL et al., 2004) and (B) $\delta^{13}C$ in peat bogs (RAJAGOPALAN et al., 1997; SUKUMAR et al., 1993) and andisols (CANET and BOURGEON 2001) from Nilgiris.

11 References

Barbiéro, L., Mohan Kumar, M. S., Violette, A., Oliva, P., Braun, J. J., Kumar, C., Furian, S., Babic, M., Riotte, J., and Valles, V., 2010. Soil transformations through ferrolysis induced by natural drainage in Vertisols of sub-humid South India. *Geoderma* **156**, 173-188.

Barbiéro, L., Parate, H. R., Descloitres, M., Bost, A., Furian, S., Kumar, M. S. M., Kumar, C., and Braun, J. J., 2007. Using a structural approach to identify relationships between soil and erosion in a semi-humid forested area, South India. *Catena* **70**, 313-329.

Berner, E. K. and Berner, R. A., 1987. *The Global Water Cycle: Geochemistry of the Environment*. Prentice-Hall, Englewood Cliffs.

Berner, R. A., 1993. Weathering and its effect on atmospheric CO2 over phanerozoic time. *Chemical Geology* **107**, 373-374.

Bischoff, J. L. and Fitzpatrick, J. A., 1991. U-Series Dating of Impure Carbonates - an Isochron Technique Using Total-Sample Dissolution. *Geochimica Et Cosmochimica Acta* **55**, 543-554.

Branca, M., Masi, U., and Voltaggio, M., 2005. An unsuccessful attempt at U/Th dating of soil calcretes from the Doukkali area (western Morocco) and environmental implications. *Chemie der Erde - Geochemistry* **65**, 347-356.

Braun, J.-J., Descloitres, M., Riotte, J., Fleury, S., BarbiÈro, L., Boeglin, J.-L., Violette, A., Lacarce, E., Ruiz, L., Sekhar, M., Mohan Kumar, M. S., Subramanian, S., and DuprÈ, B., 2009. Regolith mass balance inferred from combined mineralogical, geochemical and geophysical studies: Mule Hole gneissic watershed, South India. *Geochimica et Cosmochimica Acta* **73**, 935-961.

Braun, J.-J., Viers, J., Dupre, B., Polve, M., Ndam, J., and Muller, J.-P., 1998. Solid/Liquid REE Fractionation in the Lateritic System of Goyoum, East Cameroon: The Implication for the Present Dynamics of the Soil Covers of the Humid Tropical Regions. *Geochimica et Cosmochimica Acta* **62**, 273-299.

Brimhall, G. H., Lewis, C. J., Ford, C., Bratt, J., Taylor, G., and Warin, O., 1991. Quantitative geochemical approach to pedogenesis: importance of parent material reduction, volumetric expansion and eolian influx in laterization. *Geoderma* **51**, 51-91.

Candy, I., Black, S., and Sellwood, B. W., 2004. Quantifying time scales of pedogenic calcrete formation using U-series disequilibria. *Sedimentary Geology* **170**, 177-187.

Candy, I., Black, S., and Sellwood, B. W., 2005. U-series isochron dating of immature and mature calcretes as a basis for constructing Quaternary landform chronologies for the Sorbas basin, southeast Spain. *Quaternary Research* **64**, 100-111.

Caner, L. and Bourgeon, G., 2001. On the possibilities of palaeoenvironmental reconstitution offered by tropical highland andisols. Example of Nilgiri andisols (South India). *Comptes Rendus De L Academie Des Sciences Serie Ii Fascicule a-Sciences De La Terre Et Des Planetes* **333**, 725-731.

Capo, R. C. and Chadwick, O. A., 1999. Sources of strontium and calcium in desert soil and calcrete. *Earth and Planetary Science Letters* **170**, 61-72.

Capo, R. C., Stewart, B. W., and Chadwick, O. A., 1998. Strontium isotopes as tracers of ecosystem processes: theory and methods. *Geoderma* **82**, 197-225.

Capo, R. C., Whipkey, C. E., Blachere, J. R., and Chadwick, O. A., 2000. Pedogenic origin of dolomite in a basaltic weathering profile, Kohala peninsula, Hawaii. *Geology* **28**, 271-274.

931 Caratini, C., Fontugne, M., Pascal, J. P., Tissot, C., and Bentaleb, I., 1991. A Major Change at
932 Ca 3500 Years Bp in the Vegetation of the Western Ghats in North Kanara,
933 Karnataka. *Current Science* **61**, 669-672.
934 Chabaux, F., Dequincey, O., Leveque, J. J., Leprun, J. C., Clauer, N., Riotte, J., and Paquet,
935 H., 2003. Tracing and dating recent chemical transfers in weathering profiles by trace-
936 element geochemistry and U-238-U-234-Th-230 disequilibria: the example of the
937 Kaya lateritic toposequence (Burkina-Faso). *Comptes Rendus Geoscience* **335**, 1219-
938 1231.
939 Chiquet, A., Colin, F., Hamelin, B., Michard, A., and Nahon, D., 2000. Chemical mass
940 balance of calcrete genesis on the Toledo granite (Spain). *Chemical Geology* **170**, 19-
941 35.
942 Chiquet, A., Michard, A., Nahon, D., and Hamelin, B., 1999. Atmospheric input vs in situ
943 weathering in the genesis of calcretes: an Sr isotope study at Galvez (Central Spain).
944 *Geochimica et Cosmochimica Acta* **63**, 311-323.
945 Cole, J. M., Troyrasbury, E., Montanez, I. P., Pedone, V., Lanzirotti, A., and Hanson, G. N.,
946 2004. Petrographic and trace element analysis of uranium-rich tufa calcite, middle
947 Miocene Barstow Formation, California, USA. *Sedimentology* **51**, 433–453.
948 Dart, R. C., Barovich, K. M., Chittleborough, D. J., and Hill, S. M., 2007. Calcium in regolith
949 carbonates of central and southern Australia:Its source and implications for the global
950 carbon cycle. *Palaeogeography, Palaeoclimatology, Palaeoecology* **249**, 322-334.
951 Deniel, C. and Pin, C., 2001. Single-stage method for the simultaneous isolation of lead and
952 strontium from silicate samples for isotopic measurements. *Analytica Chimica Acta*
953 **426**, 95-103.
954 Denniston, R. F., Shearer, C. K., Layne, G. D., and Vaniman, D. T., 1997. SIMS analyses of
955 minor and trace element distributions in fracture calcite from Yucca Mountain,
956 Nevada, USA. *Geochimica et Cosmochimica Acta* **61**, 1803-1818.
957 Dequincey, O., Chabaux, F., Leprun, J. C., Paquet, H., Clauer, N., and Larque, P., 2006.
958 Lanthanide and trace element mobilization in a lateritic toposequence: inferences from
959 the Kaya laterite in Burkina Faso. *European Journal of Soil Science* **57**, 816-830.
960 Driese, S. G., Mora, C. I., Stiles, C. A., Joeckel, R. M., and Nordt, L. C., 2000. Mass-balance
961 reconstruction of a modern Vertisol: implications for interpreting the geochemistry
962 and burial alteration of paleo-Vertisols. *Geoderma* **95**, 179-204.
963 Duplessy, J. C., 1982. Glacial to Interglacial Contrasts in the Northern Indian-Ocean. *Nature*
964 **295**, 494-498.
965 Dupre, B., Dessert, C., Oliva, P., Godderis, Y., Viers, J., Francois, L., Millot, R., and
966 Gaillardet, J., 2003. Rivers, chemical weathering and Earth's climate. *Comptes Rendus*
967 *Geosciences* **335**, 1141-1160.
968 Durand, N., Ahmad, S. M., Hamelin, B., Gunnell, Y., and Curmi, P., 2006a. Origin of Ca in
969 South Indian calcretes developed on metamorphic rocks. *Journal of Geochemical*
970 *Exploration* **88**, 275-278.
971 Durand, N., Gunnell, Y., Curmi, P., and Ahmad, S. M., 2006b. Pathways of calcrete
972 development on weathered silicate rocks in Tamil Nadu, India: Mineralogy, chemistry
973 and paleoenvironmental implications. *Sedimentary Geology* **192**, 1-18.
974 Durand, N., Gunnell, Y., Curmi, P., and Ahmad, S. M., 2007. Pedogenic carbonates on
975 Precambrian silicate rocks in South India: Origin and paleoclimatic significance.
976 *Quaternary International* **162-163**, 35-49.
977 Gascoyne, M., 1983. Trace-element partition coefficients in the calcite-water system and their
978 paleoclimatic significance in cave studies. *Journal of Hydrology* **61**, 213-222.
979 Goudie, A. S., 1996. Organic agency in calcrete development. *Journal of Arid Environments*
980 **32**, 103-110.

981 Gunnell, Y. and Bourgeon, G., 1997. Soils and climatic geomorphology on the Karnataka
982 plateau, peninsular India. *CATENA* **29**, 239-262.
983 Gunnell, Y., Braucher, R., Bourles, D., and Andre, G., 2007. Quantitative and qualitative
984 insights into bedrock landform erosion on the South Indian craton using cosmogenic
985 nuclides and apatite fission tracks. *Geological Society of America Bulletin* **119**, 576-
986 585.
987 Hamidi, E. M., Colin, F., Michard, A., Boulange, B., and Nahon, D., 2001. Isotopic tracers of
988 the origin of Ca in a carbonate crust from the Middle Atlas, Morocco. *Chemical*
989 *Geology* **176**, 93-104.
990 Huang, Y. and Fairchild, I. J., 2001. Partitioning of Sr2+ and Mg2+ into calcite under karst-
991 analogue experimental conditions. *Geochimica et Cosmochimica Acta* **65**, 47-62.
992 IUSS-Working-Group-WRB, 2006. World reference base for soil resources 2006. World Soil
993 Resources FOOD AND AGRICULTURE ORGANIZATION OF THE UNITED
994 NATIONS, Rome.
995 Janardhan, A. S. and Vidal, P., 1982. Rb-Sr dating of the Gundlupet gneiss around Gundlupet,
996 Southern Karnataka. *Journal of the Geological Society of India* **23**, 578-580.
997 Kelly, M., Black, S., and Rowan, J. S., 2000. A calcrete-based U/Th chronology for landform
998 evolution in the Sorbas basin, southeast Spain. *Quaternary Science Reviews* **19**, 995-
999 1010.
1000 Lea, D. W., Mashiotta, T. A., and Spero, H. J., 1999. Controls on magnesium and strontium
1001 uptake in planktonic foraminifera determined by live culturing. *Geochimica et*
1002 *Cosmochimica Acta* **63**, 2369-2379.
1003 Lintern, M. J., Sheard, M. J., and Chivas, A. R., 2006. The source of pedogenic carbonate
1004 associated with gold-calcrete anomalies in the western Gawler Craton, South
1005 Australia. *Chemical Geology* **235**, 299-324.
1006 Lopez, O., Zuddas, P., and Faivre, D., 2009. The influence of temperature and seawater
1007 composition on calcite crystal growth mechanisms and kinetics: Implications for Mg
1008 incorporation in calcite lattice. *Geochimica et Cosmochimica Acta* **73**, 337-347.
1009 Lorens, R. B., 1981. Sr, Cd, Mn and Co distribution coefficients in calcite as a function of
1010 calcite precipitation rate. *Geochimica et Cosmochimica Acta* **45**, 553-561.
1011 Ludwig, K. R., 2003a. Mathematical-statistical treatment of data and errors for Th-230/U
1012 geochronology. *Uranium-Series Geochemistry* **52**, 631-656.
1013 Ludwig, K. R., 2003b. User's Manual for Isoplot 3.00. *Berkeley Geochronology Center*
1014 *Special Publication* **4**, 1-70.
1015 Ludwig, K. R. and Titterington, D. M., 1994. Calculation of (230)Th/U Isochrons, Ages, and
1016 Errors. *Geochimica Et Cosmochimica Acta* **58**, 5031-5042.
1017 Machette, M. N., 1985. Calcic soils of the south-western United States. *Geol. Soc. Am. Spec.*
1018 *Pap.* **203**, 1–21.
1019 Maréchal, J. C., Varma, M. R. R., Riotte, J., Vouillamoz, J. M., Kumar, M. S. M., Ruiz, L.,
1020 Sekhar, M., and Braun, J. J., 2009. Indirect and direct recharges in a tropical forested
1021 watershed: Mule Hole, India. *Journal of Hydrology* **364**, 272-284.
1022 McCall, K., Lanzirotti, A., and Rasbury, E. T., 2001. Uranium (VI) Incorporation in Paleosol
1023 Calcite: Evidence for Sequestration of U on Geologic Time Scales. In: Sciences, G. a.
1024 E. (Ed.). NSLS Activity Report.
1025 Meissner, B., Deters, P., Srikantappa, C., and Kohler, H., 2002. Geochronological evolution
1026 of the Moyar, Bhavani and Palghat shear zones of southern India: implications for east
1027 gondwana correlations. *Prec. Res.* **114**, 149-175.
1028 Naiman, Z., Quade, J., and Patchett, P. J., 2000. Isotopic evidence for eolian recycling of
1029 pedogenic carbonate and variations in carbonate dust sources throughout the
1030 southwest United States. *Geochimica et Cosmochimica Acta* **64**, 3099-3109.

1031 Naqvi, S. M. and Rogers, J. W., 1987. *Precambrian geology of India*. Clarendon Press,
1032 Oxford University Press, New york.
1033 Nehrke, G., Reichart, G. J., Van Cappellen, P., Meile, C., and Bijma, J., 2007. Dependence of
1034 calcite growth rate and Sr partitioning on solution stoichiometry: Non-Kossel crystal
1035 growth. *Geochimica et Cosmochimica Acta* **71**, 2240-2249.
1036 Netterberg, F., 1980. Geology of southern African calcretes: I.Terminology, description,
1037 macrofeatures and classification. *Transactions of the Geological Society of South*
1038 *Africa* **83**, 255–283.
1039 Neymark, L. A. and Amelin, Y. V., 2008. Natural radionuclide mobility and its influence on
1040 U-Th-Pb dating of secondary minerals from the unsaturated zone at Yucca Mountain,
1041 Nevada. *Geochimica et Cosmochimica Acta* **72**, 2067-2089.
1042 Neymark, L. A., Paces, J. B., Marshall, B. D., Peterman, Z. E., and Whelan, J. F., 2005.
1043 Geochemical and C, O, Sr, and U-series isotopic evidence for the meteoric origin of
1044 calcrete at Solitario Wash, Crater Flat, Nevada, USA. *Environmental Geology* **48**,
1045 450-465.
1046 Oh, N.-H. and Richter, D. D., 2005. Elemental translocation and loss from three highly
1047 weathered soil-bedrock profiles in the southeastern United States. *Geoderma* **126**, 5-
1048 25.
1049 Overpeck, J., Anderson, D., Trumbore, S., and Prell, W., 1996. The southwest Indian
1050 Monsoon over the last 18000 years. *Climate Dynamics* **12**, 213-225.
1051 Pal, D. K., Balpande, S. S., and Srivastava, P., 2001. Polygenetic Vertisols of the Purna
1052 Valley of Central India *Catena* **43**, 231-249
1053 Pett-Ridge, J. C., Derry, L. A., and Kurtz, A. C., 2008. Sr isotopes as a tracer of weathering
1054 processes and dust inputs in a tropical granitoid watershed, Luquillo Mountains,
1055 Puerto Rico. *Geochimica et Cosmochimica Acta* **in press**.
1056 Prabhu, C. N., Shankar, R., Anupama, K., Taieb, M., Bonnefille, R., Vidal, L., and Prasad, S.,
1057 2004. A 200-ka pollen and oxygen-isotopic record from two sediment cores from the
1058 eastern Arabian Sea. *Palaeogeography Palaeoclimatology Palaeoecology* **214**, 309-
1059 321.
1060 Prell, W. L. and Vancampo, E., 1986. Coherent Response of Arabian Sea Upwelling and
1061 Pollen Transport to Late Quaternary Monsoonal Winds. *Nature* **323**, 526-528.
1062 Pustovoytov, K., Schmidt, K., and Taubald, H., 2007. Evidence for Holocene environmental
1063 changes in the northern Fertile Crescent provided by pedogenic carbonate coatings.
1064 *Quaternary Research* **67**, 315-327.
1065 Quade, J., Chivas, A. R., and McCulloch, M. T., 1995. Strontium and carbon isotope tracers
1066 and the origins of soil carbonate in South Australia and Victoria. *Palaeogeography,*
1067 *Palaeoclimatology, Palaeoecology* **113**, 103-117.
1068 Quast, A., Hoefs, J., and Paul, J., 2006. Pedogenic carbonates as a proxy for palaeo-CO2 in
1069 the Palaeozoic atmosphere. *Palaeogeography, Palaeoclimatology, Palaeoecology* **242**,
1070 110-125.
1071 Rajagopalan, G., Sukumar, R., Ramesh, R., Pant, R. K., and Rajagopalan, G., 1997. Late
1072 Quaternary vegetational and climatic changes from tropical peats in southern India-An
1073 extended record up to 40,000 years BP. *Current Science* **73**, 60-63.
1074 Ramesh, R., 2001. High resolution Holocene monsoon records from different proxies: An
1075 assessment of their consistency. *Current Science* **81**, 1432-1436.
1076 Rech, J. A., Quade, J., and Hart, W. S., 2003. Isotopic evidence for the source of Ca and S in
1077 soil gypsum, anhydrite and calcite in the Atacama Desert, Chile. *Geochimica et*
1078 *Cosmochimica Acta* **67**, 575-586.

1079 Retallack, G. J., 1994. The environmental factor approach to the interpretation of paleosols.
1080 In: Amundson, R., et al. (Ed.), *Factors of soil formation: A fiftieth anniversary*
1081 *retrospective*. Soil Science Society of America Special Publication.
1082 Rimstidt, J. D., Balog, A., and Webb, J., 1998. Distribution of trace elements between
1083 carbonate minerals and aqueous solutions. *Geochimica et Cosmochimica Acta* **62**,
1084 1851-1863.
1085 Rosenthal, Y., Linsley, B., and Scott, A. E., 2007. PALEOCEANOGRAPHY, PHYSICAL
1086 AND CHEMICAL PROXIES | Mg/Ca and Sr/Ca Paleothermometry, *Encyclopedia of*
1087 *Quaternary Science*. Elsevier, Oxford.
1088 Rostek, F., Ruhland, G., Bassinot, F. C., Muller, P. J., Labeyrie, L. D., Lancelot, Y., and Bard,
1089 E., 1993. Reconstructing Sea-Surface Temperature and Salinity Using Delta-O-18 and
1090 Alkenone Records. *Nature* **364**, 319-321.
1091 Ruiz, L., Varma, M. R. R., Kumar, M. S. M., Sekhar, M., Marechal, J. C., Descloitres, M.,
1092 Riotte, J., Kumar, S., Kumar, C., and Braun, J. J., 2010. Water balance modelling in
1093 tropical watershed under deciduous forest (Mule Hole, India) : Regolith matric storage
1094 buffers the groundwater recharge process. *Journal of Hydrology* **380**, 460-472.
1095 Sarkar, A., 2000. High resolution Holocene monsoon record from the eastern Arabian Sea.
1096 *Earth and Planetary Science Letters* **177**, 209-218.
1097 Shadakshara Swamy, N., Jayananda, M., and Janardhan, A. S., 1995. Geochemistry of
1098 Gundlupet gneisses, Southern Karnataka: a 2.5 Ga old reworked sialic crust. In:
1099 Yoshida, M., Santosh, M., and Rao, A. T. Eds.), *India as a fragment of East*
1100 *Gondwana*. Gondwana Research Group.
1101 Singh, G., Wasson, R. J., and Agrawal, D. P., 1988. Vegetational and Seasonal Climatic
1102 Changes since the Last Full Glacial in the Thar Desert, Northwestern India*7th*
1103 *International Palynological Congress*, Brisbane, Australia.
1104 Siva Soumya, B., Sekhar, M., Riotte, J., and Braun, J.-J., 2009. Non-linear regression model
1105 for spatial variation in precipitation chemistry for South India. *Atmospheric*
1106 *Environment* **43**, 1147-1152.
1107 Srivastava, P., Bhattacharyya, T., and Pal, D. K., 2002. Significance of the formation of
1108 calcium carbonate minerals in the pedogenesis and management of cracking clay soils
1109 (vertisols) of India. *Clays and Clay Minerals* **50**, 111-126.
1110 Stephenson, A. E., DeYoreo, J. J., Wu, L., Wu, K. J., Hoyer, J., and Dove, P. M., 2008.
1111 Peptides Enhance Magnesium Signature in Calcite: Insights into Origins of Vital
1112 Effects. *Science* **322**, 724-727.
1113 Stiles, C. A., Mora, C. I., and Driese, S. G., 2001. Pedogenic iron-manganese nodules in
1114 Vertisols: A new proxy for paleoprecipitation? *Geology* **29**, 943-946.
1115 Stiles, C. A., Mora, C. I., Driese, S. G., and Robinson, A. C., 2003. Distinguishing climate
1116 and time in the soil record: Mass-balance trends in Vertisols from the Texas coastal
1117 prairie. *Geological Society of America* **31**, 331-334.
1118 Sukumar, R., Ramesh, R., Pant, R. K., and Rajagopalan, G., 1993. A ∂13C record of late
1119 Quaternary climate change from tropical peats in southern India. *Nature* **364**, 703-705.
1120 Tang, J., Kˆhler, S. J., and Dietzel, M., 2008. Sr2+/Ca2+ and 44Ca/40Ca fractionation during
1121 inorganic calcite formation: I. Sr incorporation. *Geochimica et Cosmochimica Acta*
1122 **72**, 3718-3732.
1123 Tesoriero, A. J. and Pankow, J. F., 1996. Solid solution partitioning of Sr2+, Ba2+, and Cd2+
1124 to calcite. *Geochimica et Cosmochimica Acta* **60**, 1053-1063.
1125 Tripathi, J. K. and Rajamani, V., 2007a. Geochemistry and origin of ferruginous nodules in
1126 weathered granodioritic gneisses, Mysore Plateau, Southern India. *Geochim.*
1127 *Cosmochim. Acta* **doi: 10.1016/j.gca.2007.01.001**.

1128 Tripathi, J. K. and Rajamani, V., 2007b. Geochemistry and origin of ferruginous nodules in
1129 weathered granodioritic gneisses, Mysore Plateau, Southern India. *Geochimica et*
1130 *Cosmochimica Acta* **71**, 1674-1688.
1131 Van der Hoven, S. J. and Quade, J., 2002. Tracing spatial and temporal variations in the
1132 sources of calcium in pedogenic carbonates in a semiarid environment. *Geoderma*
1133 **108**, 259-276.
1134 Vancampo, E., 1986. Monsoon Fluctuations in 2 20,000-Yr Bp Oxygen-Isotope Pollen
1135 Records Off Southwest India. *Quaternary Research* **26**, 376-388.
1136 Vancampo, E., Duplessy, J. C., and Rossignolstrick, M., 1982. Climatic Conditions Deduced
1137 from a 150-Kyr Oxygen Isotope Pollen Record from the Arabian Sea. *Nature* **296**, 56-
1138 59.
1139 Vaniman, D. T. and Chipera, S. J., 1996. Paleotransport of lanthanides and strontium recorded
1140 in calcite compositions from tuffs at Yucca Mountain, Nevada, USA. *Geochimica et*
1141 *Cosmochimica Acta* **60**, 4417-4433.
1142 Violette, A., Goddéris, Y., Maréchal, J.-C., Riotte, J., Oliva, P., Mohan Kumar, M. S., Sekhar,
1143 M., Braun, J. J. (2010) Modelling the chemical weathering fluxes at the watershed
1144 scale in the Tropics (Mule Hole, South India): Relative contribution of the
1145 smectite/kaolinite assemblage versus primary minerals. *Chemical Geology*,
1146 doi:10.1016/j.chemgeol.2010.07.009.
1147 Wang, Y., Nahon, D., and Merino, E., 1994. Dynamic model of the genesis of calcretes
1148 replacing silicate rocks in semi-arid regions. *Geochimica et Cosmochimica Acta* **58**,
1149 5131-5145.
1150 Whipkey, C. E., Capo, R. C., Hsieh, J. C. C., and Chadwick, O. A., 2002. Development of
1151 magnesian carbonates in Quaternary soils on the island of Hawaii. *Journal of*
1152 *Sedimentary Research* **72**, 158-165.
1153 Wieder, M. and Yaalon, D. H., 1974. Effect of matrix composition on carbonate nodule
1154 crystallization. *Geoderma* **11**, 95-121.
1155 Wieder, M. and Yaalon, D. H., 1982. Micromorphological fabrics and developmental stages
1156 of carbonate nobular forms related to soil characteristics. *Geoderma* **28**, 203-220.
1157
1158

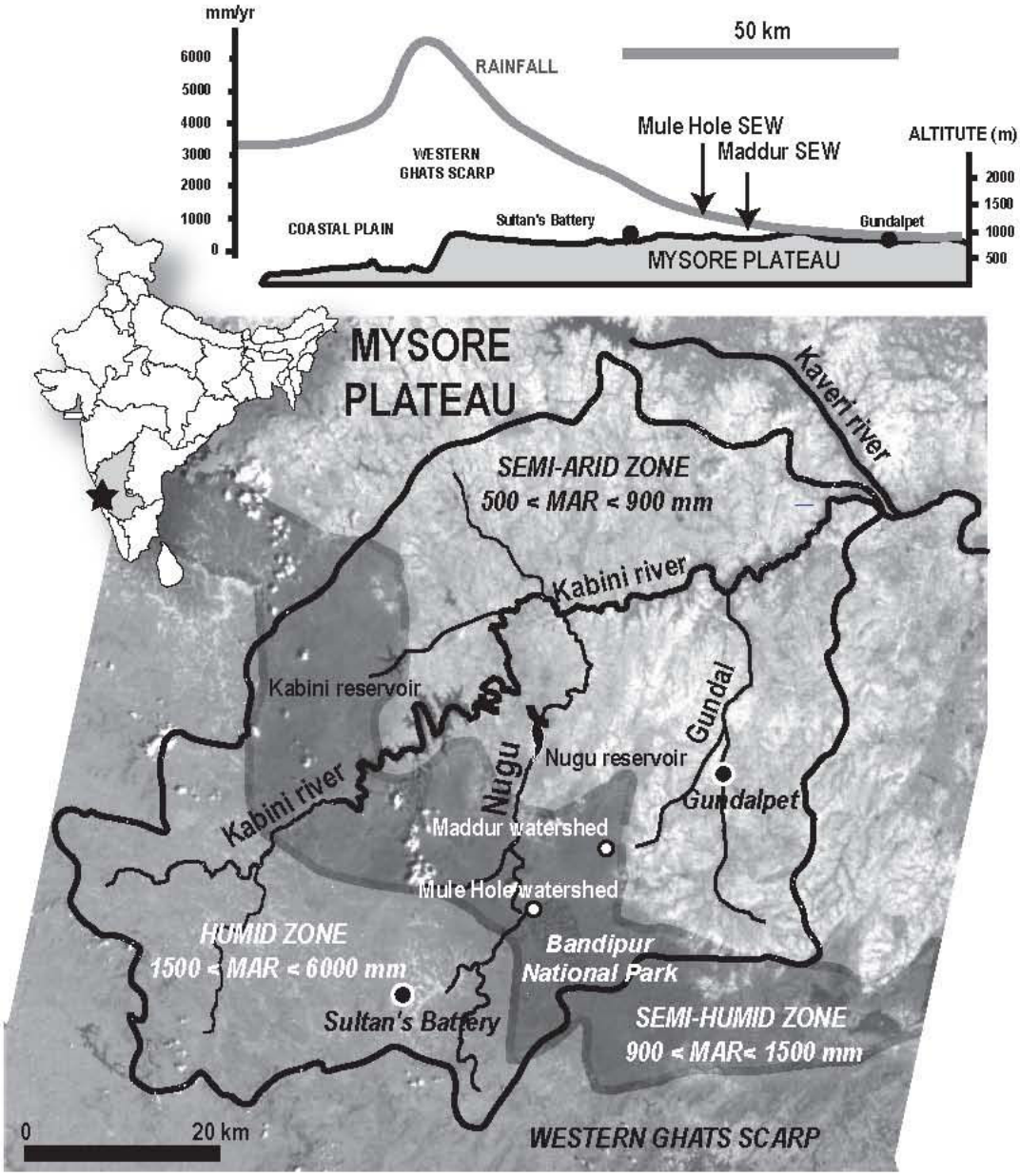

Violette et al., FIGURE 1

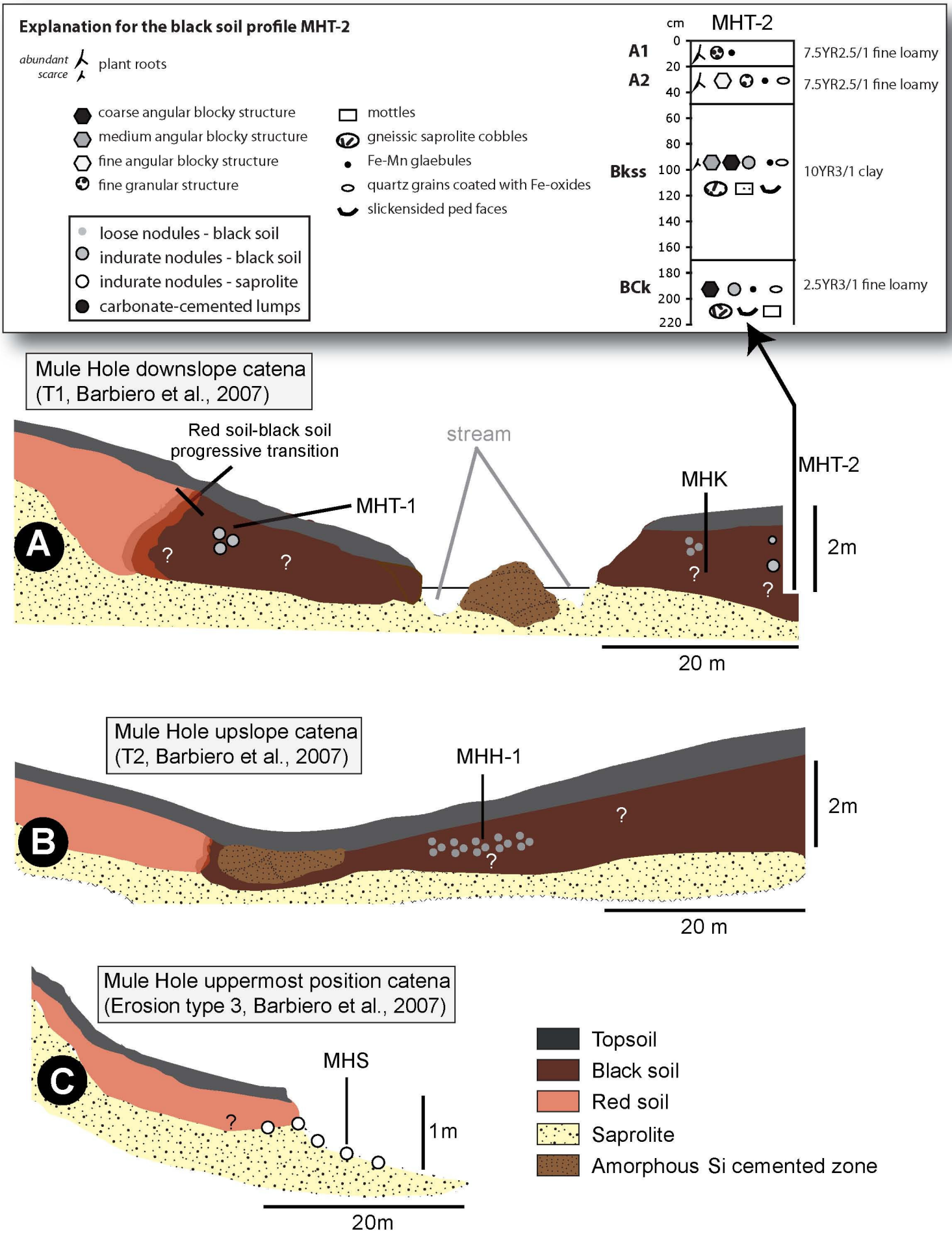

FIGURE 2 Violette et al.

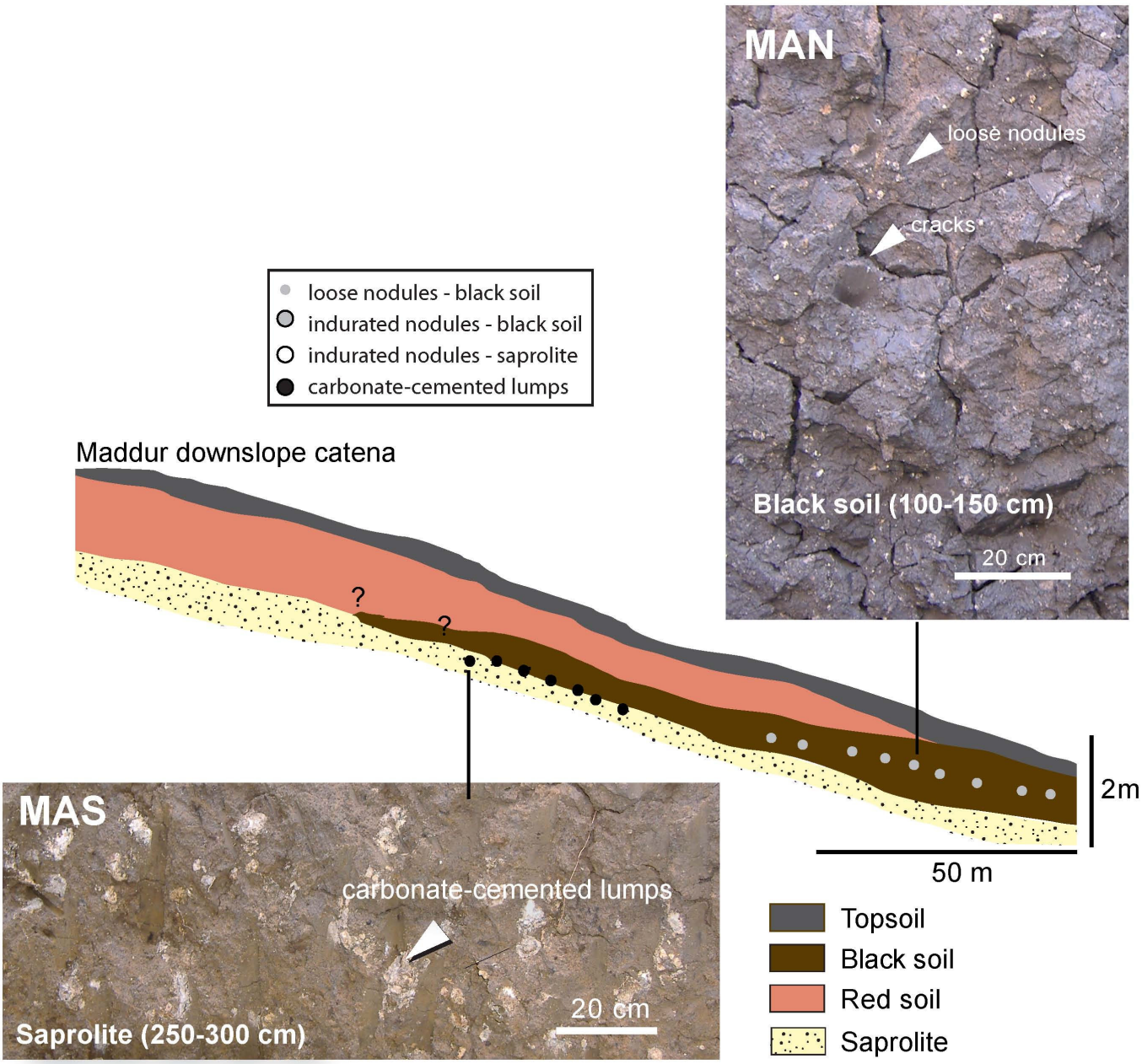

FIGURE 3 Violette et al.

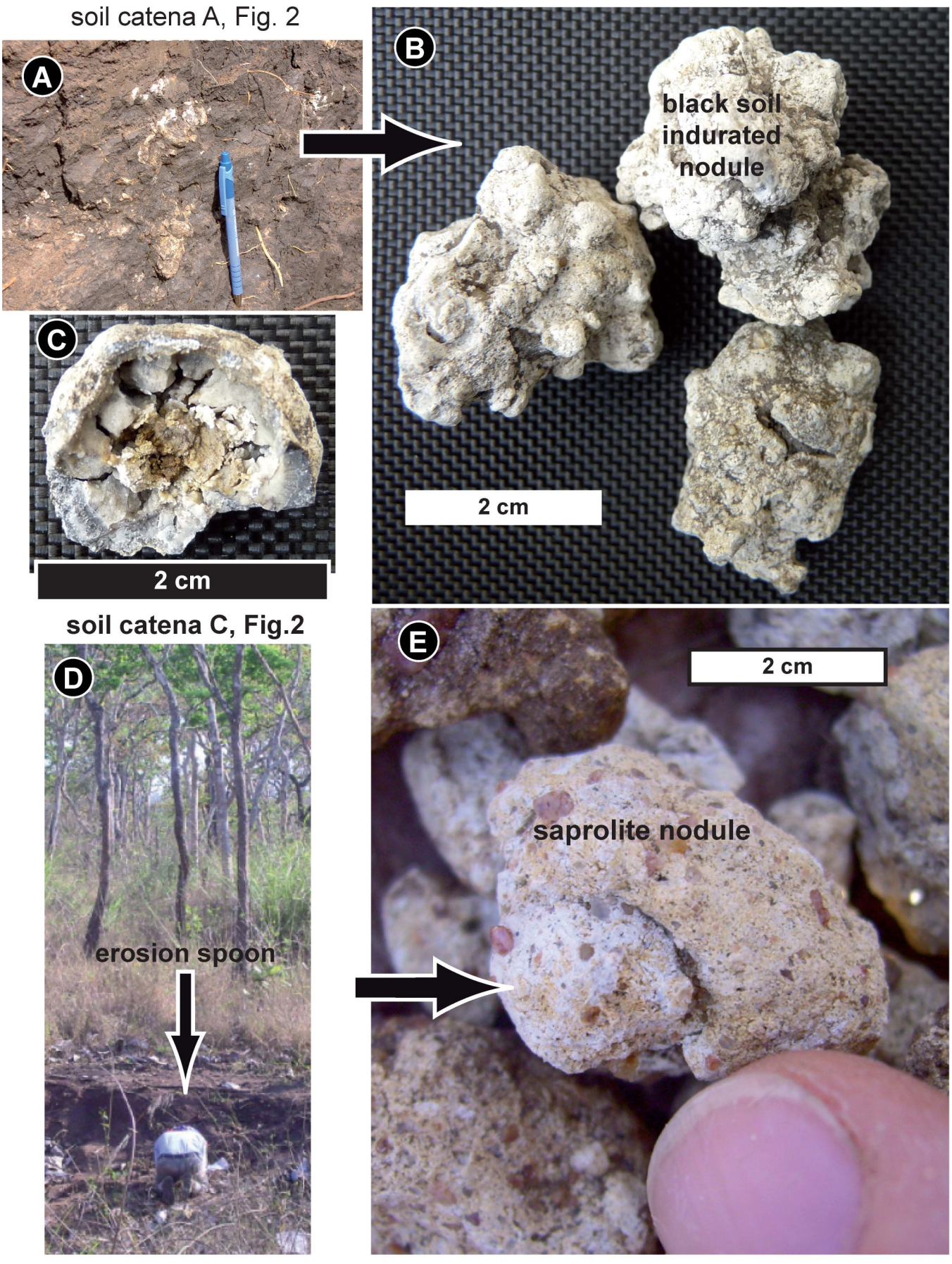

FIGURE 4 Violette et al.

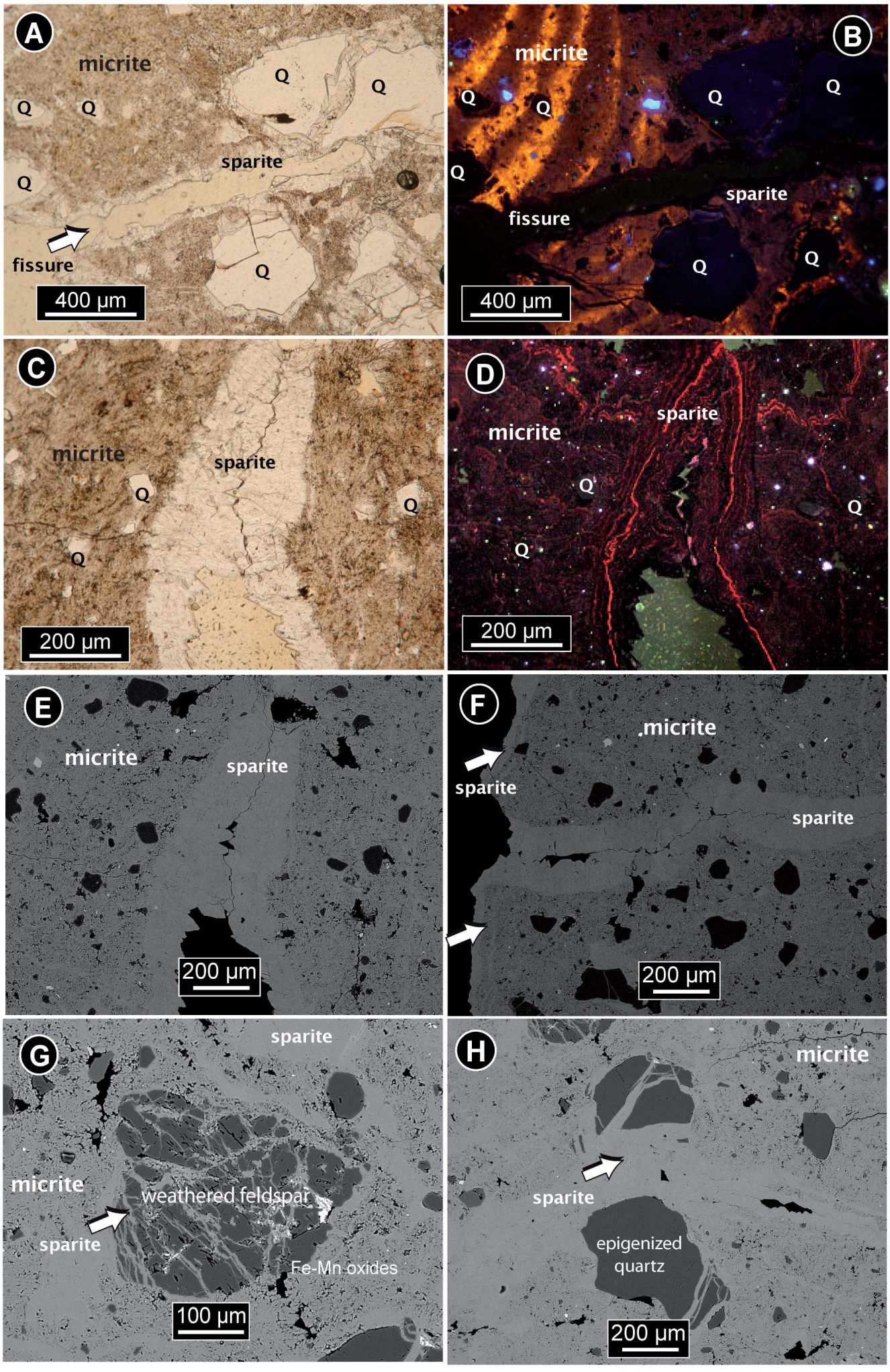

Figure 5, Violette et al.

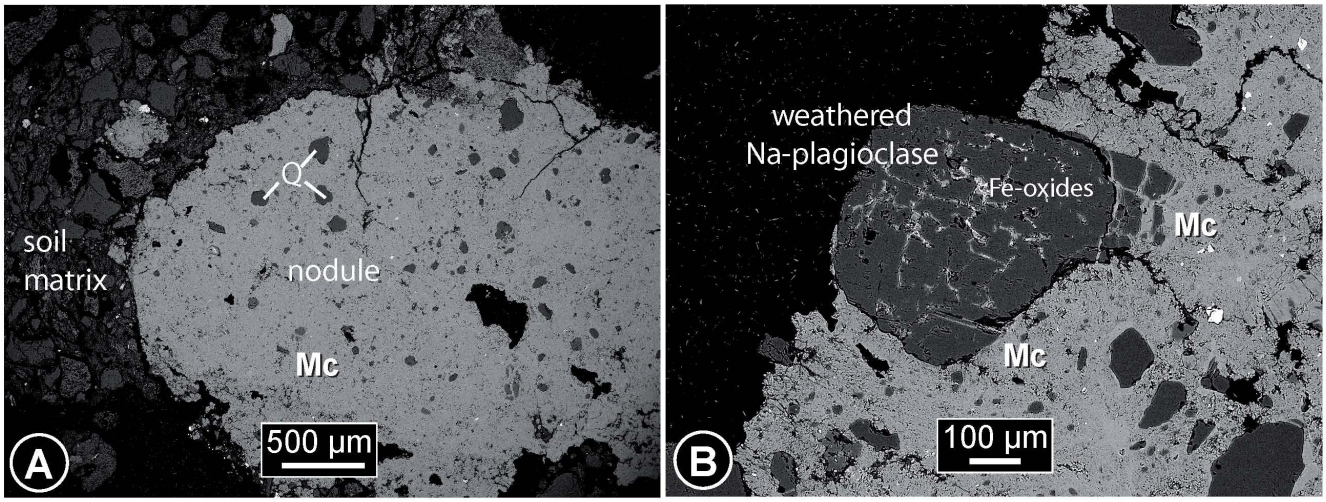

Figure 6, Violette et al.

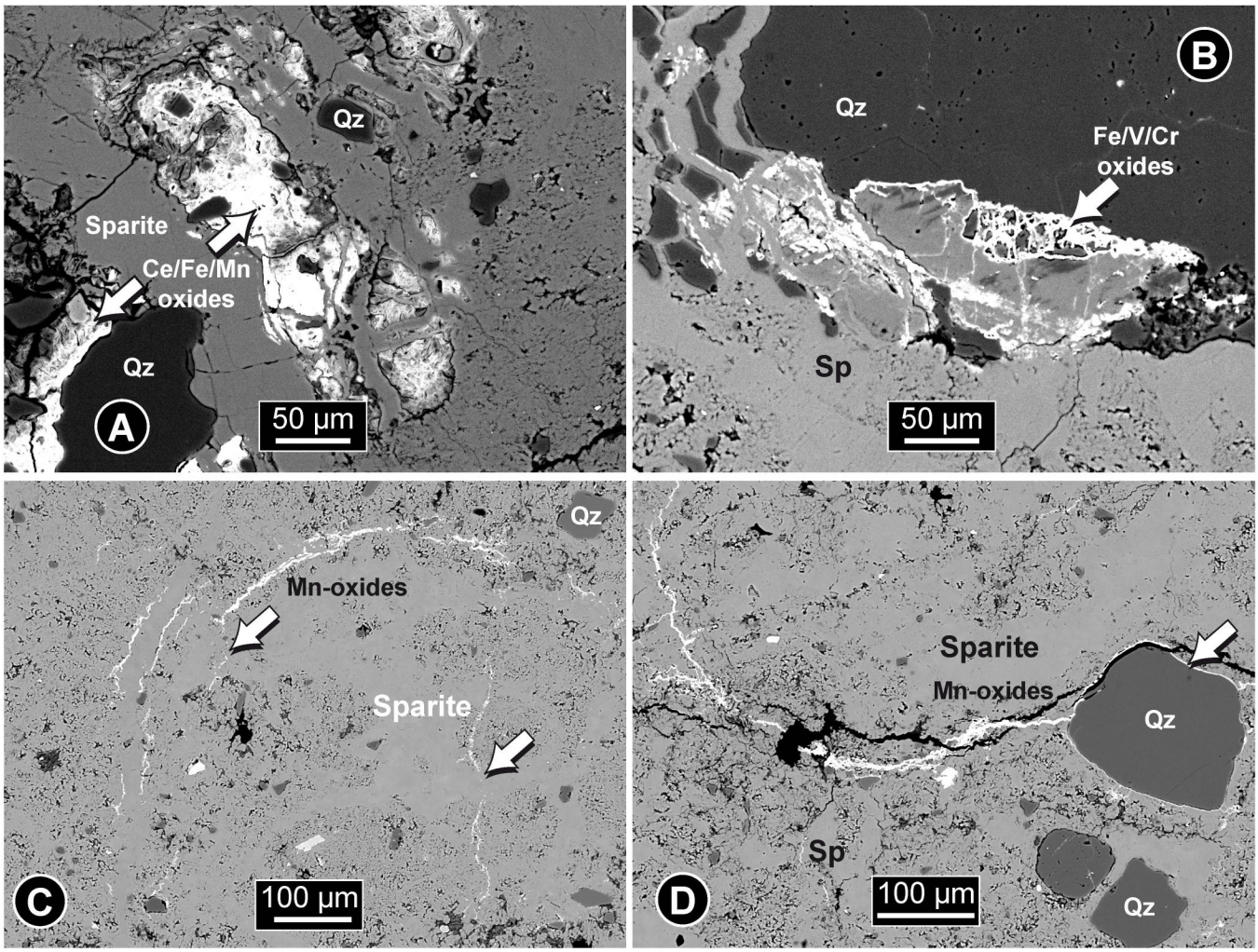

Figure 7, Violette et al.

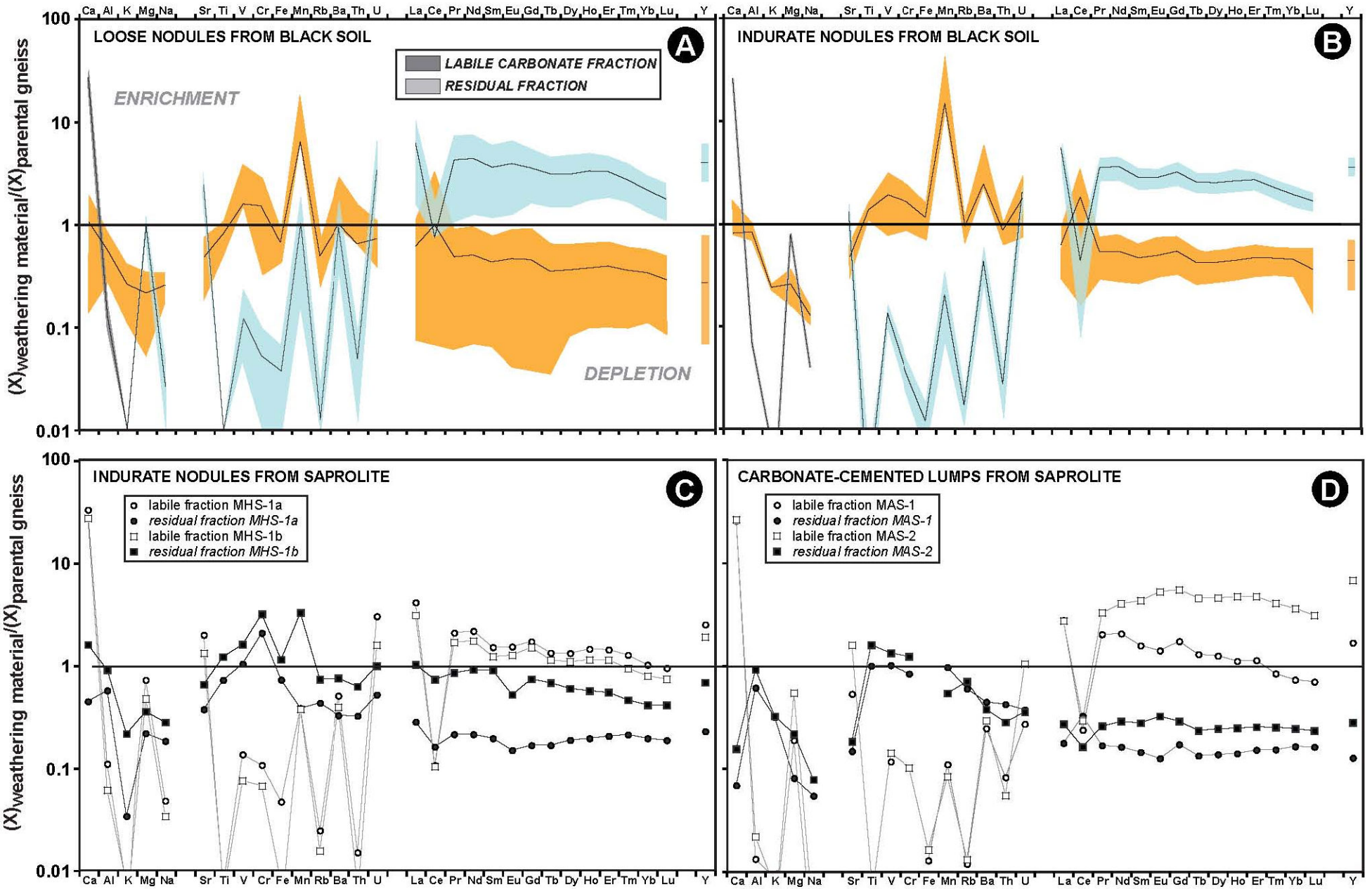

Figure 8, Violette et al.

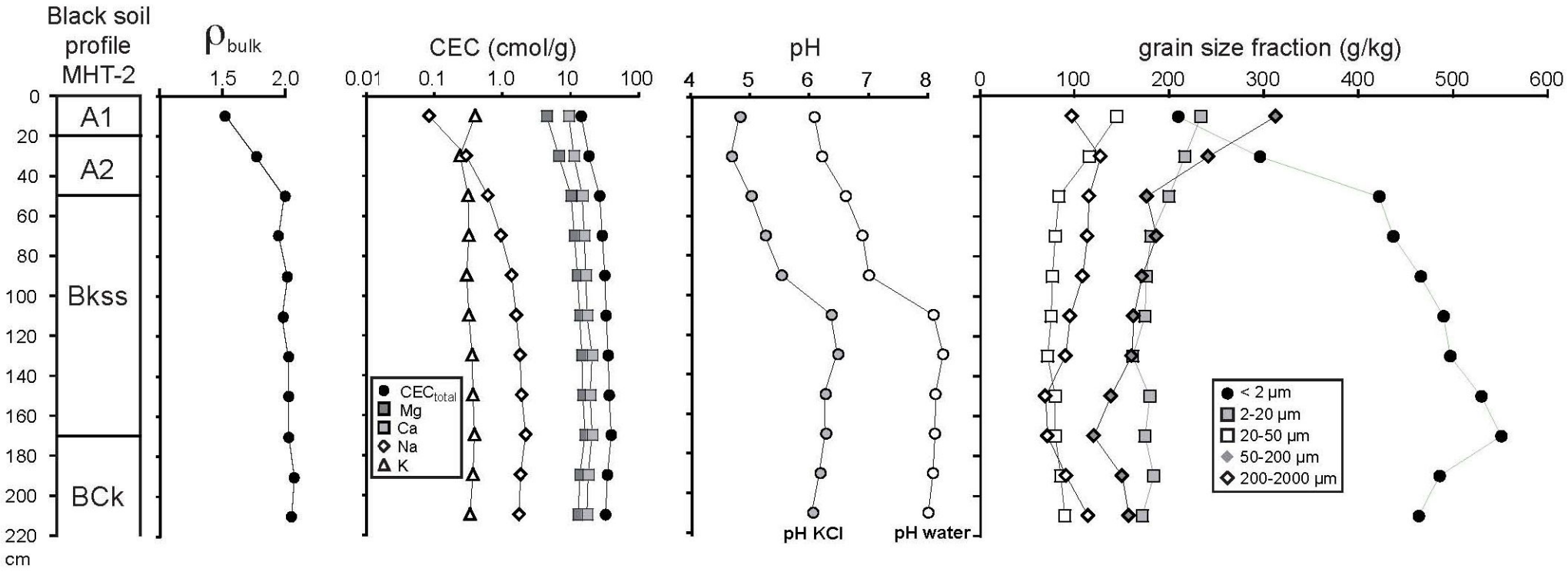

Violette et al. Figure 9

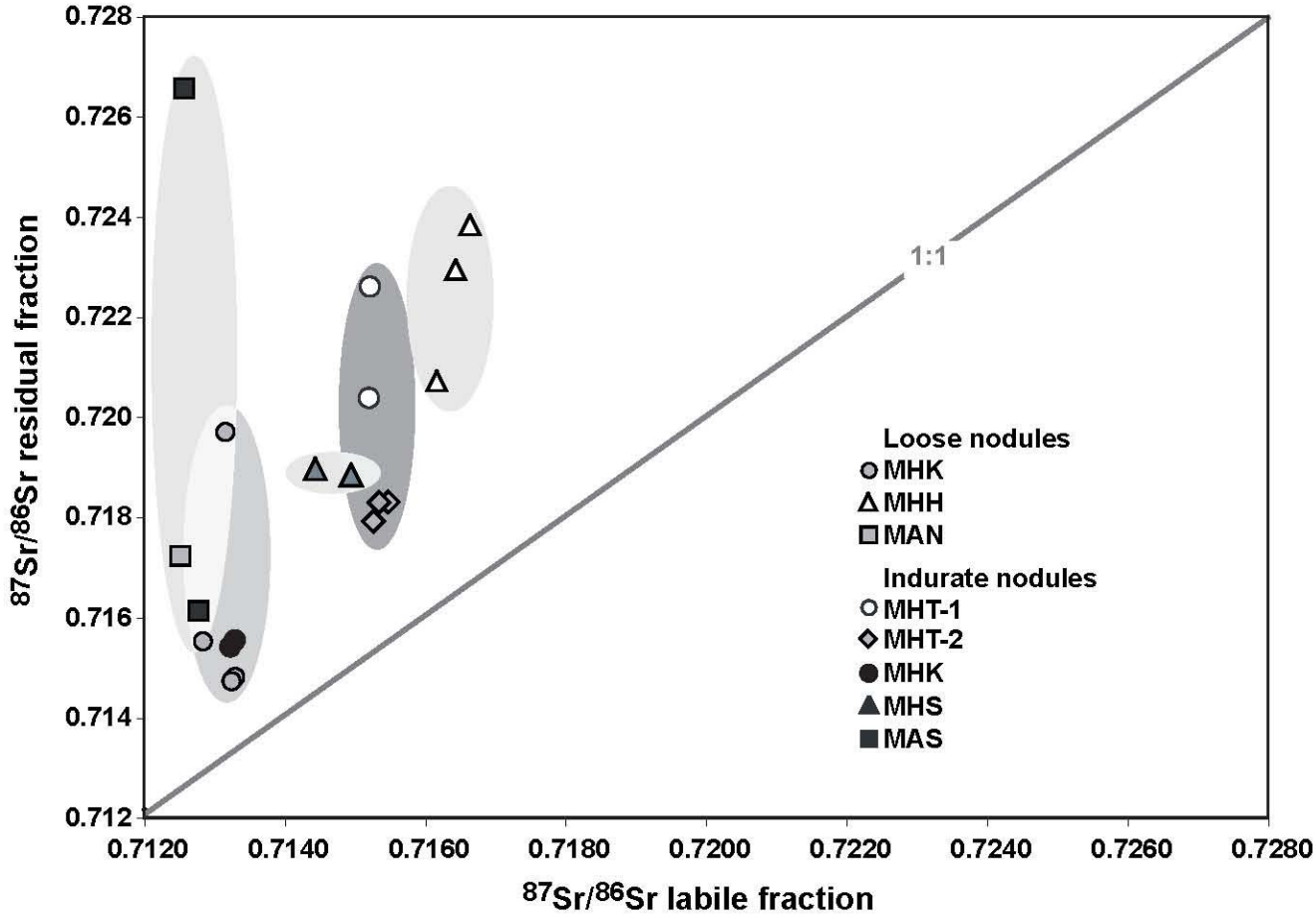

FIGURE 10 Violette et al.

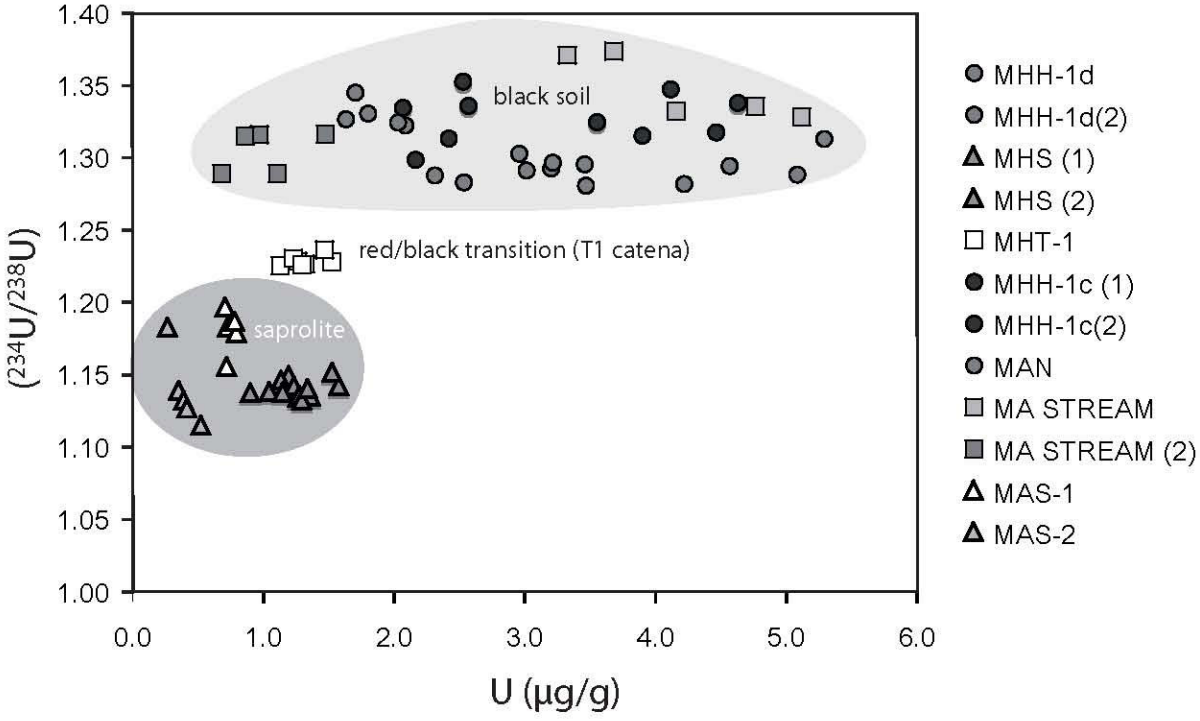

Figure 11, Violette et al.

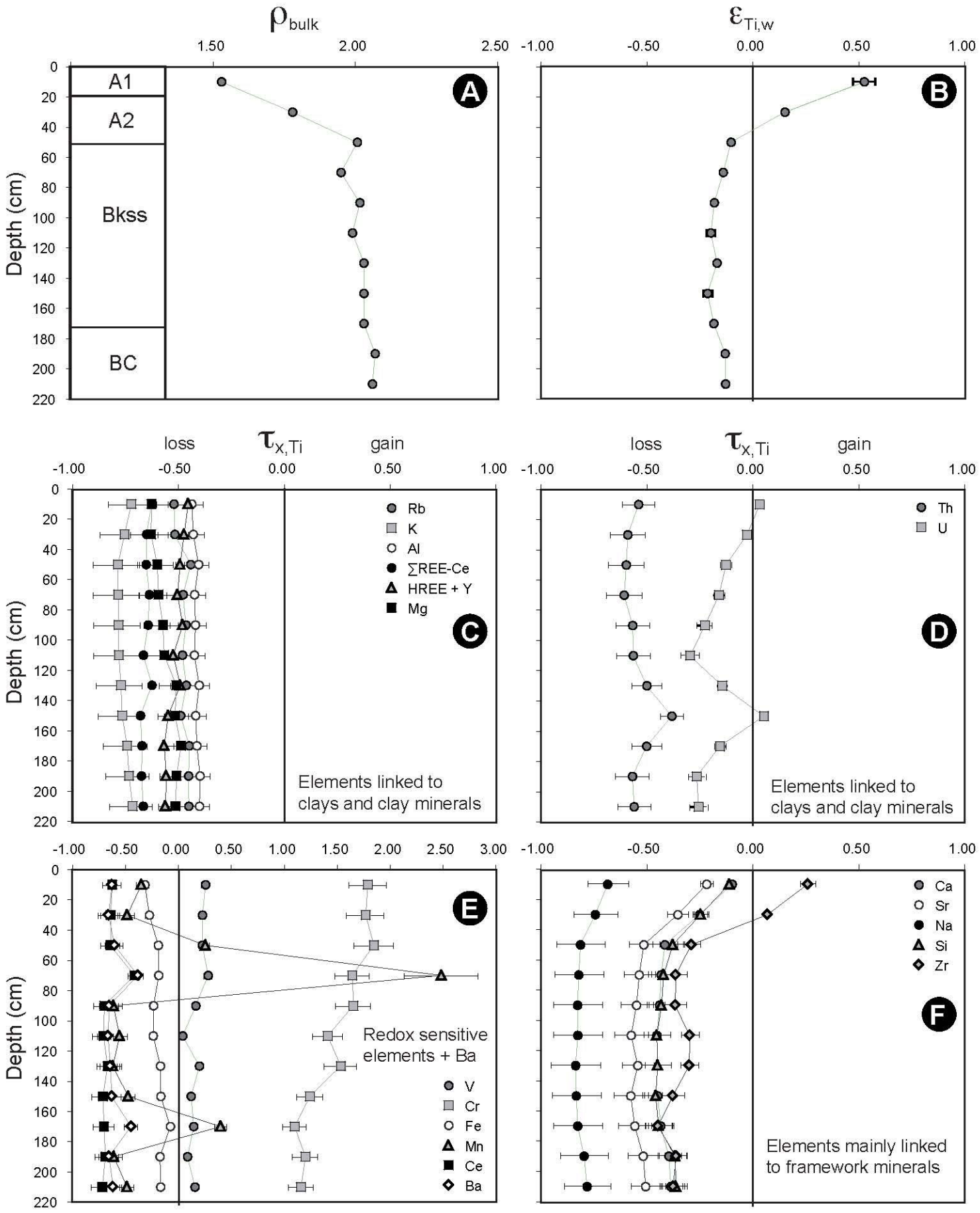

Violette et al. Figure 12

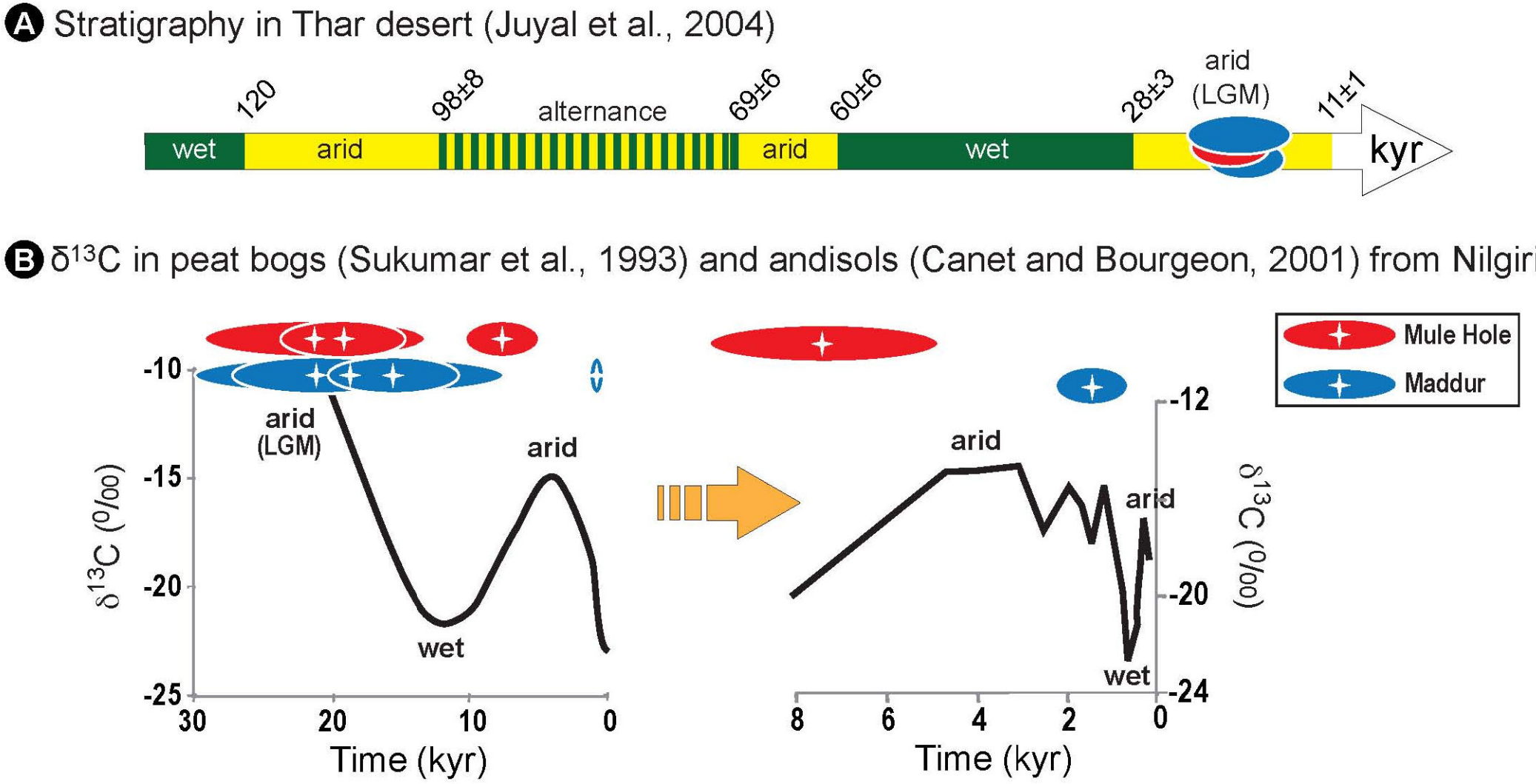

FIGURE 13 Violette et al.

Table 1

	depth	Grain size fraction (g/kg)					$Ca_{exchange}$	$Mg_{exchange}$	$K_{exchange}$	$Na_{exchange}$	ρ_{bulk}	SD	SiO2	Al2O3	Fe2O3	MnO	MgO	CaO	Na2O	K2O	TiO2	P2O5
	cm	< 2 µm	2-20 µm	20-50 µm	50-200 µm	200-2000 µm	cmol/kg	cmol/kg	cmol/kg	cmol/kg	g/cm^3		wt%	wt%	wt%	wt%	wt%	wt%	wt%	wt%	wt%	wt%
bulk matrices																						
MHT-2	**0-20**	210	234	145	313	98	10	4.6	0.4	0.1	1.5	0.04	73	9.3	2.9	0.03	0.88	1.6	1.8	0.51	0.40	
MHT-2	**20-40**	296	217	116	242	128	11	6.9	0.2	0.3	1.8	0.03	71	11	3.5	0.03	1.0	1.5	1.7	0.52	0.45	
MHT-2	**40-60**	422	200	84	177	116	15	10	0.3	0.6	2.0	0.06	66	13	4.4	0.08	1.2	1.4	1.4	0.51	0.51	
MHT-2	**60-80**	437	181	80	187	114	16	12	0.3	1.0	2.0	0.10	66	13	4.8	0.24	1.3	1.4	1.4	0.55	0.55	
MHT-2	**80-100**	466	176	77	172	109	17	13	0.3	1.4	2.0	0.05	66	14	4.6	0.03	1.4	1.4	1.4	0.57	0.56	
MHT-2	**100-120**	490	175	76	163	96	18	14	0.3	1.6	2.0	0.03	66	14	4.7	0.03	1.5	1.4	1.5	0.59	0.58	
MHT-2	**120-140**	497	162	72	161	91	21	15	0.4	1.9	2.0	0.04	63	14	4.8	0.03	1.6	2.9	1.3	0.58	0.55	
MHT-2	**140-160**	530	180	80	139	70	20	16	0.4	2.0	2.0	0.03	65	14	5.1	0.04	1.7	1.5	1.4	0.63	0.58	
MHT-2	**160-180**	551	175	80	121	72	21	17	0.4	2.3	2.0	0.05	64	14	5.5	0.10	1.7	1.4	1.4	0.67	0.56	
MHT-2	**180-200**	486	184	86	151	92	19	14	0.4	1.9	2.1	0.04	68	13	4.5	0.03	1.5	1.4	1.5	0.64	0.51	
MHT-2	**200-220**	464	172	90	158	115	18	13	0.3	1.8	2.1	0.03	68	13	4.6	0.03	1.5	1.4	1.6	0.68	0.51	

		Sr	Ti	V	Cr	Ba	Rb	Zr	Th	U	La	Ce	Pr	Nd	Sm	Eu	Gd	Tb	Dy	Ho	Er	Tm	Yb	Lu
		µg/g	µg/g	µg/g	µg/g	µg/g	µg/g	µg/g	µg/g	µg/g	µg/g	µg/g	µg/g	µg/g	µg/g	µg/g	µg/g	µg/g	µg/g	µg/g	µg/g	µg/g	µg/g	µg/g
bulk matrices																								
MHT-2	**0-20**	202	2367	62	280	113	27	271	5.1	1.01	19	36	4.2	16	3.2	0.87	2.8	0.44	2.7	0.55	1.6	0.24	1.6	0.26
MHT-2	**20-40**	190	2697	69	317	118	31	262	5.2	1.09	20	40	4.6	18	3.7	0.99	3.3	0.53	3.1	0.62	1.7	0.26	1.8	0.29
MHT-2	**40-60**	163	3069	79	371	156	40	198	5.8	1.11	23	45	5.1	19	3.9	1.0	3.5	0.56	3.3	0.67	1.9	0.28	1.9	0.30
MHT-2	**60-80**	167	3296	88	370	262	40	190	6.1	1.15	26	79	5.7	21	4.3	1.1	3.9	0.60	3.6	0.70	2.0	0.30	2.1	0.32
MHT-2	**80-100**	165	3350	82	378	149	42	193	6.8	1.07	26	41	5.7	22	4.4	1.1	3.9	0.62	3.7	0.73	2.1	0.31	2.1	0.33
MHT-2	**100-120**	161	3464	75	355	149	42	221	7.1	1.01	25	41	5.6	21	4.3	1.1	3.8	0.61	3.6	0.72	2.1	0.32	2.1	0.33
MHT-2a*	**100-110**	174	3473	85	317	157	43	<DL	6.7	0.79	25	52	5.6	21	4.2	1.1	4.7	0.61	3.6	0.70	2.0	0.32	1.8	0.26
MHT-2b*	**110-130**	167	3295	84	301	150	43	<DL	6.4	0.82	20	29	4.7	18	3.7	1.0	4.0	0.53	3.2	0.61	1.8	0.25	1.6	0.23
MHT-2	**120-140**	163	3278	82	353	150	41	208	7.7	1.2	26	44	5.8	22	4.4	1.1	3.8	0.60	3.6	0.71	2.0	0.30	2.0	0.32
MHT-2	**140-160**	160	3464	81	330	164	41	196	10.0	1.5	24	41	5.4	21	4.2	1.1	3.7	0.59	3.5	0.68	1.9	0.28	2.0	0.31
MHT-2	**160-180**	161	3338	80	298	236	43	168	7.8	1.2	23	40	5.2	20	4.0	1.0	3.4	0.55	3.2	0.63	1.8	0.27	1.8	0.29
MHT-2	**180-200**	162	3075	70	287	136	39	178	6.2	0.94	21	39	4.8	18	3.7	0.94	3.2	0.50	3.0	0.60	1.7	0.26	1.7	0.27
MHT-2c*	**140-200**	156	3187	79	292	135	40	<DL	6.2	0.85	20	33	4.6	18	3.8	0.94	3.9	0.53	3.1	0.58	1.7	0.23	1.5	0.22
MHT-2	**200-220**	166	3081	75	282	151	40	175	6.4	0.95	22	35	4.9	19	3.7	0.98	3.2	0.51	3.0	0.59	1.7	0.26	1.7	0.27

Table 2

	depth (cm)	% CaCO3 nodule*	Ca µg/g	Al µg/g	K µg/g	Mg µg/g	Na µg/g	Sr µg/g	Ti µg/g	V µg/g	Cr µg/g	Fe µg/g	Mn µg/g	Rb µg/g	Ba µg/g	Zr µg/g	Th µg/g	U µg/g	La µg/g	Ce µg/g	Pr µg/g	Nd µg/g	Sm µg/g	Eu µg/g	Gd µg/g	Tb µg/g	Dy µg/g	Ho µg/g	Er µg/g	Tm µg/g	Yb µg/g	Lu µg/g	Y µg/g	∑LREE-Ce	∑HREE	Ce/Ce*	La/Sm	$^{87}Sr/^{86}Sr$	2σ (10^{-6})
LOOSE NODULES FROM BLACK SOIL																																					
HCl-labile fraction																																					
MHK-1a	**0-40**	62	541200	17079	< DL	16652	1040	745	24.5	23.4	10.1	955	327.3	1.8	122	0.3	1.0	4.3	488	293	82	315	51	12	27.0	4.4	30	5.9	15	1.8	8.6	0.92	183	974	66	0.36	1.5	0.712828	8
MHK-1b	**0-40**	73	384681	8971	< DL	13428	488	571	7.6	11.2	< DL	< DL	371.6	0.6	523	0.2	0.3	3.3	100	52	15	61	10	2.5	8.4	1.3	8.6	1.9	5.4	0.73	3.7	0.48	74	197	22	0.33	1.5	0.713148	8
MHK-1c	**0-40**	72	375197	4821	< DL	13169	1752	541	3.8	10.7	3.2	< DL	388.6	0.7	451	0.1	0.4	2.8	110	60	17	67	11	2.8	6.8	1.1	9.4	1.8	5.5	0.68	3.3	0.42	75	215	22	0.34	1.5	NA	
MHK-2a	**0-40**	63	378487	9349	< DL	13136	NA	452	0.3	8.5	26.5	2908	401.2	0.7	110	0.1	0.5	1.9	418	72	65	254	40	12	36	4.5	26	5.3	13	1.5	7.6	1.0	178	825	59	0.11	1.6	0.713285	9
MHK-2b	**0-40**	56	544752	13361	< DL	21523	NA	813	7.6	8.0	4.2	< DL	768.8	0.7	541	0.2	0.4	3.1	234	86	36	145	24	6.4	25	3.3	19	4.2	11.5	1.4	7.6	1.0	148	471	48	0.23	1.5	0.713238	7
MHK-2c	**0-40**	65	393641	4900	< DL	14748	1651	545	5.3	6.6	3.7	< DL	340.7	0.5	522	0.1	0.4	2.0	144	51	22	90	15	4.1	18	2.2	12	2.4	7.2	0.90	4.6	0.57	94	293	30	0.22	1.5	NA	
MHH-1a	**0-100**	63	468525	13363	< DL	13672	146	497	22.9	8.7	13.8	3354	97.7	2.4	170	0.3	0.1	7.6	173	26	25	101	17	3.9	16	2.2	13	2.7	7.6	1.0	4.8	0.60	108	336	32	0.10	1.6	0.716170	10
MHH-1b	**0-100**	82	378193	13046	< DL	10059	84	295	16.1	3.3	9.0	762	263	1.5	77	0.1	0.2	3.7	228	9	33	126	19	4.5	17	2.1	12	2.4	6.4	0.79	4.1	0.57	88	426	28	0.03	1.9	0.715981	26
MHH-1c	**0-100**		NA	NA	NA	NA	NA	638	< DL	6.5	3.4	< DL	65	0.4	158	< DL	0.9	6.1	316	25	43	170	28	6.4	24	3.1	18	3.8	10.1	1.2	5.8	0.68	128	587	43	0.05	1.8	NA	
MHH-1d	**0-100**		NA	NA	NA	NA	NA	349	< DL	1.5	1.7	< DL	58	0.2	66	< DL	1.2	4.0	193	9	26	104	16	3.9	14	1.8	10	2.3	6.1	0.74	3.7	0.47	85	357	25	0.03	1.9	NA	
MHH-2a	**surface**	63	455178	19438	< DL	20437	479	727	9.8	8.4	9.9	1737	92	1.0	229	< DL	0.3	5.4	790	26	116	432	63	15	49	5.8	31	5.9	15	1.7	8.6	1.0	199	1465	69	0.02	2.0	0.716642	7
MHH-2b	**surface**	73	385730	15866	< DL	14136	863	429	13.8	2.4	6.1	574	9.7	1.4	101	0.1	0.1	2.6	175	7	21	83	12	3.2	10	1.3	7.7	1.7	4.6	0.57	3.0	0.39	76	305	19	0.03	2.3	0.716661	8
MHH-2c	**surface**	72	381311	10121	< DL	15662	458	453	13.3	4.4	7.3	672	5.3	1.6	121	0.2	0.3	2.9	251	14	35	131	20	4.5	19	2.4	13	2.6	7.3	1.0	4.7	0.66	103	460	31	0.04	2.0	0.716436	7
MHH-2d	**surface**	77	381562	4921	< DL	15618	1709	445	6.2	2.7	5.9	449	8.0	1.1	112	< DL	0.2	2.9	158	10	19	77	11	2.3	11	1.3	7.7	1.6	4.4	0.5	2.8	0.37	67	278	19	0.04	2.1	NA	
MHK-3a	**surface**	71	391615	9626	< DL	21724	319	679	14.5	6.8	9.4	2102	588	0.9	158	0.1	0.2	2.1	199	58	32	129	22	6.2	23	3.0	18	3.7	10	1.3	7.4	1.0	136	411	45	0.18	1.4	0.713244	8
MHK-3b	**surface**	77	390778	8425	< DL	16586	288	562	1.8	6.3	3.2	264	785	0.5	332	0.2	0.2	2.3	78	36	13	51	9	2.3	8.7	1.2	6.8	1.4	4.1	0.5	2.7	0.34	55	161	17	0.28	1.4	0.713179	10
MHK-3c	**surface**	77	393358	4893	< DL	15809	892	562	8.2	6.2	1.2	1234	787	0.6	329	0.2	0.2	2.3	79	36	13	50	9	2.0	11.6	1.4	6.8	1.4	4.4	0.5	3.0	0.38	55	165	18	0.27	1.4	0.713182	7
MHK-3d	**surface**	84	375120	6778	< DL	12602	1539	491	3.8	6.6	3.3	686	930	0.6	362	0.1	0.3	2.4	130	48	19	76	13	3.2	18	2.0	9.8	2.1	5.9	0.76	4.4	0.58	80	260	26	0.23	1.6	NA	
MAN-1	**0-100**		387537	726	< DL	8668	313	834	< DL	16.5	< DL	560	553	0.3	267	0.1	1.1	5.7	197	152	35	137	25	6.0	24	3.2	17	3.4	9.6	1.3	7.2	1.1	102	423	43	0.44	1.2	0.712511	12
HCl-residual fraction																																					
MHK-1a	**0-40**		37135	60202	1324	5183	9769	170	2160	54	379	28865	217	23	105	31	9.2	0.70	50	61	9.0	34	5.4	1.4	3.7	0.53	3.1	0.64	1.7	0.23	1.2	0.13	24	104	7.5	0.70	1.5	0.715539	8
MHK-1b	**0-40**		2616	17541	2828	555	7787	26	1474	71	124	21583	1275	17	70	54	0.66	0.58	1.2	8.6	0.26	1.0	0.19	0.07	0.16	0.02	0.12	0.03	0.07	0.01	0.09	0.01	0.5	2.9	0.4	3.7	0.95	0.719714	43
MHK-1c	**0-40**		17846	46588	2913	4313	12865	179	1407	45	100	16058	1050	20	302	38	3.5	0.47	15	35	2.6	10	1.9	0.49	1.4	0.20	1.2	0.25	0.71	0.10	0.59	0.09	7.9	31	3.1	1.4	1.2	NA	
MHK-2a	**0-40**		35856	49296	56	3828	9161	144	1512	37	437	25364	231	18	89	36	5.8	0.53	52	67	8.6	34	5.3	1.4	3.8	0.52	3.1	0.64	1.7	0.22	1.1	0.12	22	105	7.4	0.77	1.5	0.714826	11
MHK-2b	**0-40**		11842	26965	1555	2876	5450	63	973	30	64	14326	1048	11	186	19	1.5	0.25	7.7	11	1.4	5.5	1.0	0.22	0.72	0.10	0.64	0.14	0.39	0.05	0.30	0.05	4.2	16	1.7	0.79	1.3	0.714743	7
MHH-1a	**0-100**		9573	71431	4893	4769	9885	126	2564	75	605	38795	189	42	111	52	5.4	0.70	16	18	2.8	11	2.0	0.29	1.6	0.21	1.3	0.26	0.79	0.11	0.63	0.08	9.2	34	3.4	0.65	1.2	0.720717	9
MHH-1b	**0-100**		22621	31783	3745	2207	9811	162	1985	38	136	15460	101	25	99	42	5.5	0.63	23	18	3.9	15	2.6	0.65	1.9	0.27	1.6	0.34	1.0	0.14	0.82	0.12	10	47	4.3	0.45	1.4	NA	
MHH-2a	**surface**		12941	36669	7694	1423	8048	115	2122	44	299	26693	147	41	119	24	7.7	0.64	60	22	9.5	36	5.1	1.3	4.0	0.42	2.3	0.45	1.2	0.13	0.80	0.10	9.9	116	5.4	0.22	1.8	0.723832	12
MHH-2b	**surface**		123	6568	5987	< DL	4116	2.9	1167	25	84	14656	37	22	17	20	0.10	0.28	0.05	2.5	0.01	0.03	0.01	0.00	0.00	0.00	0.01	0.00	0.00	0.00	0.00	0.00	0.0	0.1	0.0	34	0.80	NA	
MHH-2c	**surface**		11562	33227	4724	2435	7422	104	1260	26	91	12116	67	25	85	22	3.1	0.37	14	7.2	2.2	9.0	1.4	0.35	1.1	0.16	0.91	0.19	0.54	0.09	0.45	0.06	6.3	28	2.4	0.31	1.5	0.722937	8
MHH-2d	**surface**		25886	63591	7094	4868	10513	153	2201	51	181	25831	104	55	147	44	5.9	1.21	52	16	7.1	28	4.1	1.1	5.0	0.56	3.0	0.57	1.7	0.21	1.3	0.18	22	97	7.5	0.20	2.0	0.722495	
MHK-3a	**surface**		37675	60396	3352	5248	11164	187	2211	51	447	27589	664	27	145	38	6.8	0.65	30	35	5.3	22	3.7	0.85	2.7	0.4	2.5	0.53	1.6	0.20	1.3	0.16	20	64	6.7	0.67	1.3	0.715579	9
MHK-3b	**surface**		1557	17169	2819	466	4274	28	1449	81	91	15740	7003	14	603	26	0.80	0.35	2.4	31	0.4	1.4	0.2	0.1	0.2	0.02	0.14	0.03	0.08	0.01	0.07	0.01	0.9	4.7	0.4	7.5	1.7	0.715490	11
MHK-3c	**surface**		47	11378	2604	< DL	4081	1.0	1490	86	95	16089	7257	14	9	28	0.03	0.35	0.0	31	0.00	0.01	0.00	0.00	0.05	0.00	0.00	0.00	0.00	0.00	0.00	0.00	0.0	0.1	0.0	2066	0.51	NA	
MHK-3d	**surface**		8598	50017	1563	4505	8511	124	1983	154	136	28093	< DL	27	40	33	4.6	0.46	18	80	3.0	11	1.7	0.31	1.4	0.19	1.2	0.25	0.76	0.10	0.63	0.10	7.6	35	3.2	2.7	1.6	NA	
MAN-1			5739	69244	5358	8444	4645	89	3738	557	120	< DL	15469	54	1939	54	33	1.19	44	737	9.6	36.5	6.5	1.8	9.5	0.90	4.4	0.83	2.4	0.32	2.1	0.31	19	108	11	9	1.0	0.717241	16
INDURATE NODULES FROM BLACK SOIL																																					
HCl-labile fraction																																					
MHT-1a	**130-150**	81	393440	5760	< DL	12264	1179	333	3.3	6.7	3.4	437	43	0.7	100	0.01	0.13	1.7	216	15	31	121	19	4.4	18	2.3	14	2.8	7.9	1.0	5.6	0.78	100	410	34	0.04	1.7	0.715189	7
MHT-1b	**130-150**	60	395858	4970	< DL	12374	1585	320	9.4	6.8	3.8	507	23	1.4	84	0.01	0.18	1.6	181	9.2	26	100	16	3.6	16	1.9	11	2.3	6.5	0.79	4.6	0.62	82	341	28	0.03	1.8	0.715078	7
MHT-1c	**130-150**	77	407382	4151	< DL	13042	913	320	5.5	10	4.2	0	85	1.0	113	0.02	0.10	1.6	195	12	28	106	17	3.8	15	1.9	11	2.2	6.1	0.76	4.2	0.56	79	364	26	0.04	1.8	0.715200	7
MHT-2a	**100-110**	70	386547	NA	NA	NA	NA	322	8.7	8.4	7.2	517	49	1.1	78	<DL	0.42	1.5	310	75	40	148	22	5.1	24	2.6	14	2.7	7.9	0.89	5.3	0.66	105	550	34	0.16	2.2	0.715480	12
MHT-2b	**110-130**	84	352866	NA	NA	NA	NA	215	<DL	6.1	<DL	483	74	0.7	73	<DL	0.31	1.3	229	52	30	115	17	3.8	18	2.1	12	2.3	6.2	0.73	4.4	0.56	91	412	28	0.15	2.1	0.715345	10
MHT-2c	**140-200**	86	352547	NA	NA	NA	NA	191	1.7	6.3	<DL	399	152	0.5	179	<DL	0.26	1.7	133	31	18	68	11	2.6	11	1.3	7.5	1.5	4.4	0.54	2.9	0.41	62	243	19	0.15	2.0	0.715265	12
HCl-residual fraction																																					
MHT-1a	**100-150**		33744	70791	3491	5173	4423	84	3118	75	120	33132	1178	68	235	43	9.5	0.83	45	52	7.5	29	4.7	1.0	3.5	0.50	2.9	0.59	1.7	0.23	1.5	0.20	20	91	7.6	0.68	1.5	0.720397	8
MHT-1c	**100-150**		6500	53300	3176	2964	3505	49	2523	56	99	25067	1081	53	244	44	7.5	0.58	20	35	3.6	14	2.3	0.49	1.7	0.23	1.5	0.31	0.85	0.12	0.78	0.12	8.5	42	3.9	0.99	1.4	0.722616	7
MHT-2a	**100-110**		5150	NA	NA	NA	NA	107	2818	67	273	26479	198	32	83	44	4.8	2.1	14	54	2.6	9.4	1.7	0.45	1.9	0.22	1.3	0.25	0.79	0.12	0.76	<DL	6.9	29	3.5	2.20	1.2	0.718295	9
MHT-2b	**110-130**		6138	NA	NA	NA	NA	142	3603	133	311	44461	2688	44	300	54	6.7	1.1	15	229	3.1	12	2.2	0.58	3.0	0.30	1.7	0.33	1.0	0.15	0.94	0.13	8.3	35	4.5	8.1	1.1	0.718288	12
MHT-2c	**140-200**		6068	NA	NA	NA	NA	129	3922	208	291	58413	22746	50	2114	60	6.8	2.5	27	299	4.9	18	3.0	0.88	4.3	0.41	2.2	0.44	1.3	0.19	1.3	0.19	11	58	6.0	6.3	1.4	0.717911	10
INDURATE NODULES FROM SAPROLITE																																					
HCl-labile fraction																																					
MHS-1a	**surface**	57	477435	7971	< DL	11331	1482	445	13	7.8	15	1568	139	1.3	127	0.04	0.13	2.4	164	8.0	18	68	9.3	2.2	9.4	1.1	6.2	1.3	3.6	0.46	2.4	0.35	62	270	15	0.04	2.7	0.714443	8
MHS-1b	**surface**	71	394847	4404	< DL	7473	1052	298	11	4.3	9.2	112	136	0.86	99	0.03	0.09	1.3	123	7.8	14	54	7.5	1.8	8.2	0.9	5.1	1.0	2.8	0.34	1.9	0.27	47	209	12	0.05	2.5	0.714948	8
HCl-residual fraction																																					
MHS-1a	**surface**		6460	41310	472	3437	5670	84	1721	59	286	24277	139	24	82	29	2.8	0.41	11.2	12	1.8	6.7	1.2	0.21	0.9	0.14	0.88	0.18	0.5	0.08	0.47	0.07	5.6	22	2.3	0.66	1.5	0.718957	16
MHS-1b	**surface**		23100	65844	2991	5611	8624	146	2890	92	436	38182	1179	40	188	44	5.5	0.79	40	55	7.2	29	5.5	0.74	4.0	0.56	2.8	0.51	1.4	0.17	1.0	0.15	17	86	6.5	0.79	1.1	0.718836	17
CARBONATE-CEMENTED LUMPS FROM SAPROLITE																																					
HCl-labile fraction																																					
MAS-1	**300**	61	370604	955	< DL	2963	13	119	<DL	6.7	<DL	428	40	0.65	61	<DL	0.72	0.22	109	18	17	64	9.7	2.0	9.5	1.1	5.9	1.0	2.8	0.3	1.7	0.26	41	212	13.1	0.10	1.8	0.712564	11
MAS-2	**300**	65	379272	1577	< DL	8601	83	358	6.6	8.1	14	543	30	0.72	73	<DL	0.48	0.8	108	22	28	125	26	7.4	30	3.7	22	4.2	12	1.5	8.6	1.14	167	324	52	0.10	0.64	0.712770	12
HCl-residual fraction																																					
MAS-1	**300**		994	44300	4390	1271	1685	33	2377	58	115	<DL	349	33	111	37	3.7	0.30	7.0	24	1.4	5.1	0.89	0.18	0.94	0.11	0.64	0.13	0.38	0.06	0.39	0.06	3.1	15	1.8	1.9	1.2	0.726572	15
MAS-2	**300**		2250	66512	4480	3416	2413	41	3800	76	168	<DL	196	39	94	25	2.5	0.28	10.8	12	2.2	9.0	1.7	0.5	1.6	0.19	1.2	0.22	0.63	0.09	0.59	0.09	6.9	26	3.0	0.61	0.98	0.716142	15
AVERAGE PARENTAL GNEISS			14429	72421	13847	15697	30899	224	2377	57	137	33443	361	55	250	172	8.8	0.80	40	75	8.4	31	6.1	1.4	5.5	0.82	4.7	0.90	2.5	0.36	2.4	0.37	24	92	12.0	1.00	1.00	0.713174	15

Table 3

	Cl mg/L	Ca mg/L	K mg/L	Mg mg/L	Na mg/L	Al µg/L	Sr µg/L	Fe µg/L	Mn µg/L	Th ng/L	U ng/L	La ng/L	Ce ng/L	Pr ng/L	Nd ng/L	Sm ng/L	Eu ng/L	Gd ng/L	Tb ng/L	Dy ng/L	Ho ng/L	Er ng/L	Tm ng/L	Yb ng/L	Lu ng/L	Y ng/L	87Sr/86Sr
Mule Hole rainwater																										
June 2003-September 2007																										
Mean	1.15	1.05	0.44	0.18	0.45	1.61	3.6	1.1	4.0	1.09	0.60	4.00	9.27	1.43	6.52	2.34	1.84	1.70	0.62	1.25	0.48	1.08	0.68	1.22	0.52	5.9	0.713945
SD	2.06	1.11	1.24	0.21	0.52	1.15	4.0	2.5	2.7	0.93	0.43	3.15	5.99	0.83	3.28	1.40	3.13	1.97	0.55	1.24	0.55	1.08	0.84	1.12	0.65	3.24	0.003645
Min	0.04	0.06	<dl	0.01	<dl	0.44	0.5	<dl	1.5	0.19	0.06	0.15	2.17	0.54	2.06	0.81	0.15	0.05	0.27	0.36	0.08	0.32	0.09	0.53	0.10	1.62	0.708751
Max	23.2	7.10	11.9	0.92	2.48	4.5	13.8	5.7	10.0	3.18	1.41	10.8	21.5	2.82	12.8	5.20	6.5	5.9	1.44	4.6	1.54	3.21	1.27	3.92	1.27	9.7	0.718439
n	194	194	194	194	194	10	10	10	10	10	10	10	10	10	10	10	10	10	10	10	10	10	10	10	10	10	8

Table 4

	^{238}U µg/g	2σ	^{232}Th µg/g	2σ	(232/238)	2σ	(230/238)	2σ	(234/238)	2σ	Age kyr	+/-	MSWD
MHH-1d (1)											1.3	0.8	0.73
1	3.201	0.015	1.685	0.006	0.172	0.002	0.124	0.006	1.293	0.010			
2	3.213	0.012	2.172	0.008	0.221	0.002	0.151	0.008	1.297	0.008			
3	2.311	0.011	2.779	0.010	0.393	0.004	0.265	0.013	1.288	0.009			
4	2.955	0.013	1.335	0.005	0.148	0.001	0.110	0.005	1.303	0.008			
5	2.532	0.013	2.460	0.010	0.318	0.003	0.217	0.011	1.283	0.011			
6	3.011	0.016	2.031	0.007	0.221	0.002	0.152	0.008	1.291	0.011			
MHH-1d (2)											-0.8	2	2.7
1	3.457	0.016	1.554	0.008	0.147	0.001	0.103	0.005	1.296	0.009			
2	4.567	0.027	1.633	0.009	0.117	0.001	0.080	0.004	1.294	0.011			
3	4.220	0.022	1.838	0.010	0.143	0.001	0.098	0.005	1.282	0.010			
4	3.468	0.022	1.415	0.007	0.134	0.001	0.100	0.005	1.281	0.011			
5	5.082	0.033	1.704	0.008	0.110	0.001	0.075	0.004	1.289	0.012			
6	5.290	0.035	1.631	0.008	0.101	0.001	0.068	0.003	1.313	0.012			
MHS (1)											18	12	10.8
1	1.582	0.012	1.235	0.041	0.256	0.009	0.230	0.025	1.142	0.012			
2	1.365	0.008	1.743	0.007	0.418	0.004	0.238	0.014	1.135	0.011			
3	1.048	0.007	1.473	0.006	0.460	0.005	0.302	0.018	1.138	0.011			
4	1.191	0.006	1.422	0.005	0.391	0.004	0.318	0.016	1.137	0.010			
5	0.906	0.004	1.236	0.005	0.447	0.004	0.321	0.016	1.137	0.009			
6	1.531	0.007	1.409	0.005	0.301	0.003	0.297	0.015	1.151	0.010			
7	1.200	0.005	1.041	0.004	0.284	0.003	0.235	0.012	1.149	0.008			
8	1.141	0.005	1.315	0.005	0.377	0.004	0.277	0.014	1.146	0.009			
MHS (2)											22	6.5	8.2
1	1.267	0.005	1.356	0.006	0.350	0.004	0.276	0.008	1.134	0.007			
2	1.239	0.005	1.176	0.005	0.311	0.003	0.239	0.007	1.142	0.006			
3	1.282	0.006	2.068	0.010	0.528	0.005	0.278	0.008	1.135	0.008			
4	1.154	0.005	1.219	0.007	0.346	0.003	0.275	0.008	1.137	0.007			
5	1.298	0.005	1.469	0.008	0.370	0.004	0.270	0.008	1.132	0.007			
6	1.344	0.005	1.289	0.006	0.314	0.003	0.245	0.007	1.140	0.007			
MHT-1											16	4.8	1.5
1	1.320	0.008	1.797	0.059	0.446	0.015	0.350	0.020	1.226	0.011			
2	1.524	0.009	1.764	0.058	0.379	0.013	0.326	0.019	1.228	0.011			
3	1.470	0.009	2.265	0.074	0.504	0.017	0.378	0.022	1.236	0.011			
4	1.265	0.009	1.902	0.062	0.492	0.016	0.339	0.019	1.228	0.012			
5	1.131	0.005	2.313	0.009	0.669	0.007	0.438	0.022	1.225	0.008			
6	1.232	0.006	1.997	0.008	0.530	0.005	0.384	0.019	1.230	0.010			
7	1.295	0.006	2.096	0.008	0.529	0.005	0.402	0.020	1.226	0.009			
MHH-1c (1)											2	2	26
1	3.897	0.014	1.817	0.006	0.153	0.002	0.102	0.005	1.315	0.007			
2	4.463	0.023	2.124	0.007	0.156	0.002	0.112	0.006	1.318	0.011			
3	2.417	0.014	1.715	0.006	0.232	0.002	0.148	0.007	1.313	0.012			
4	2.163	0.023	1.794	0.007	0.271	0.003	0.173	0.009	1.299	0.020			
5	4.116	0.019	2.288	0.008	0.182	0.002	0.128	0.006	1.347	0.010			
MHH-1c (2)											5.2	4.8	14
1	3.552	0.015	1.794	0.010	0.165	0.002	0.116	0.006	1.325	0.008			
2	4.630	0.024	1.916	0.011	0.135	0.001	0.121	0.006	1.338	0.010			
3	2.067	0.010	1.874	0.010	0.297	0.003	0.186	0.009	1.335	0.009			
4	2.527	0.012	1.679	0.009	0.217	0.002	0.122	0.006	1.353	0.009			
5	2.567	0.012	1.682	0.008	0.214	0.002	0.138	0.007	1.336	0.009			
MAN											7.5	2.7	2
1	1.704	0.007	1.497	0.006	0.287	0.003	0.265	0.008	1.345	0.013			
2	1.802	0.007	1.797	0.007	0.326	0.003	0.294	0.009	1.331	0.013			
3	2.085	0.009	2.036	0.013	0.319	0.003	0.299	0.009	1.322	0.013			
4	2.031	0.008	2.334	0.014	0.376	0.004	0.330	0.010	1.324	0.013			
5	1.633	0.007	2.061	0.013	0.413	0.004	0.342	0.010	1.327	0.013			
MA ST											18	5.0	6.1
1	4.763	0.022	1.779	0.007	0.122	0.001	0.242	0.007	1.335	0.011			
2	4.160	0.024	1.747	0.007	0.137	0.001	0.264	0.008	1.332	0.013			
3	3.325	0.016	1.878	0.007	0.185	0.002	0.276	0.008	1.371	0.011			
4	5.115	0.023	1.494	0.006	0.096	0.001	0.239	0.007	1.328	0.010			
5	3.683	0.015	1.667	0.006	0.148	0.001	0.250	0.007	1.374	0.010			
MA ST											22	8	3.1
1	1.474	0.006	1.647	0.006	0.366	0.004	0.386	0.019	1.316	0.013			
2	0.971	0.004	1.465	0.005	0.494	0.005	0.377	0.019	1.316	0.013			
3	0.862	0.004	1.422	0.005	0.540	0.005	0.421	0.021	1.315	0.013			
4	1.108	0.004	2.637	0.010	0.778	0.008	0.512	0.026	1.289	0.013			
5	0.681	0.003	1.449	0.005	0.696	0.007	0.473	0.024	1.289	0.013			
MAS-1											66	65	15
1	0.710	0.003	1.521	0.006	0.701	0.007	0.787	0.039	1.196	0.008			
2	0.723	0.003	2.060	0.008	0.933	0.009	0.737	0.037	1.155	0.007			
3	0.733	0.003	1.357	0.005	0.606	0.006	0.767	0.038	1.183	0.007			
4	0.800	0.003	1.393	0.007	0.570	0.006	0.618	0.031	1.179	0.007			
5	0.785	0.003	1.635	0.007	0.681	0.007	0.732	0.037	1.186	0.007			
MAS-2											60	53	3.5
1	0.356	0.002	2.881	0.012	2.651	0.027	1.136	0.034	1.139	0.023			
2	0.271	0.001	2.043	0.008	2.463	0.025	1.042	0.031	1.183	0.024			
3	0.395	0.002	3.210	0.015	2.658	0.027	1.139	0.034	1.132	0.023			
4	0.525	0.002	4.559	0.018	2.839	0.028	1.141	0.034	1.115	0.022			
5	0.421	0.002	4.239	0.017	3.295	0.033	1.237	0.037	1.127	0.023			